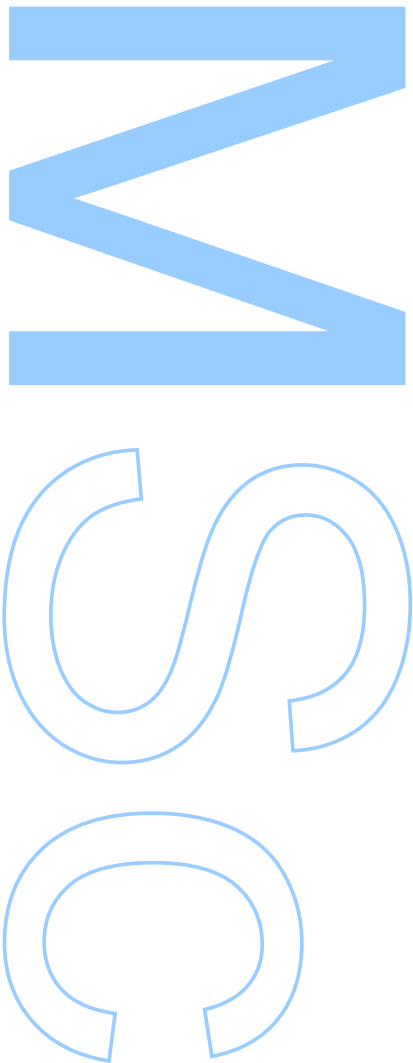
New advanced fiber optic microstructures

Paulo Manuel Ribeiro Robalinho
Mestrado Integrado em Engenharia Física
Departamento de Física e Astronomia
2019

Orientador
Orlando José dos Reis Frazão, Professor Auxiliar Convidado, Faculdade de Ciências



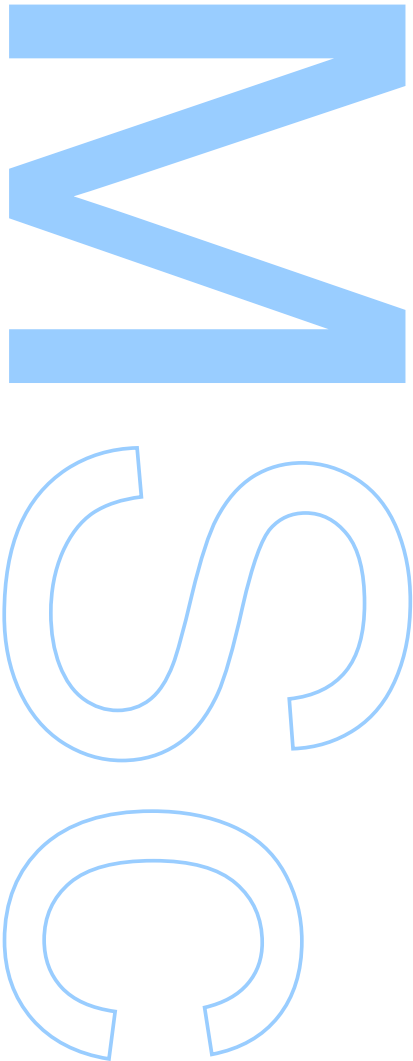
U.PORTO

FACULDADE DE CIÊNCIAS
UNIVERSIDADE DO PORTO

Todas as correções determinadas pelo júri, e só essas, foram efetuadas.

O Presidente do Júri,

Porto, _____/_____/_____



UNIVERSIDADE DO PORTO

MASTERS THESIS

New advanced fiber optic microstructures

Author:
Paulo ROBALINHO

Supervisor:
Orlando FRAZÃO

A thesis submitted in fulfilment of the requirements
for the degree of MSc. Engineering Physics

at the

Faculdade de Ciências da Universidade do Porto
Departamento de Física e Astronomia

November 7, 2019

" No great mind has ever existed without a touch of madness "

Aristotle

Acknowledgements

In the execution of this thesis, thank my parents for their support, the help of Professor Orlando Jose Reis Frazao, my supervisor, for the orientation throughout the thesis, Professor Ariel Guerreiro for the help in the simulations of the operation of the optical structures and Catarina Silva Monteiro and Carlos Gaspar Pacheco for the technical support.

UNIVERSIDADE DO PORTO

Abstract

Faculdade de Ciências da Universidade do Porto
Departamento de Física e Astronomia

MSc. Engineering Physics

New advanced fiber optic microstructures

by Paulo ROBALINHO

This thesis consists in the study of new structures at the optical fiber end in order to develop new optical sensors. This work focuses on the understanding of the microsphere's functioning as a dispersive element that will lead to the generation of optical modes as well as the potential of the microsphere when coupled with other structures. This study begins with the presentation of several simulations where contemplates the theoretical case and the cases that can more easily appear in experimental practice. Next is presented a curvature sensor that reveals to be interferometric allowed two reading modes: in intensity and in wavelength shift. Then a fiber optic cantilever that reveals two modes of operation, contact and proximity, allowing to evaluate a given surface as well as the vibration.

Finally, several microstructures with little participation in the scientific literature are studied in terms of the index variation of a liquid and the temperature variation. The structures are tips with drop, cylindrical and conical geometries in addition to structures that are composed by microspheres in series with tip. The longer and thinner structures are the most sensitive.

Keywords: Optical Fiber Sensor, Microsphere, Curvature sensor, Cantilever, Taper.

UNIVERSIDADE DO PORTO

Resumo

Faculdade de Ciências da Universidade do Porto
Departamento de Física e Astronomia

Mestrado Integrado em Engenharia Física

Novas microestruturas avançadas em fibra óptica

por Paulo ROBALINHO

Esta tese consiste no estudo de novas estruturas na ponta da fibra óptica com o objetivo de desenvolver novos sensores ópticos. Este trabalho incide na compreensão do funcionamento da microesfera como elemento dispersivo que levará à criação de modos ópticos assim como as potencialidades da microsfera quando acopladas a outras estruturas. O estudo inicia-se com a apresentação de várias simulações que contemplam o caso teórico e os casos que mais facilmente podem aparecer na prática experimental. Em seguida é apresentado um sensor de curvatura que revela ser interferométrico e que pode ser interrogado como sensor de intensidade e em comprimento de onda. Depois um cantiléver em fibra óptica que revela dois modos de operação, contacto e de proximidade, permitindo avaliar uma dada superfície assim como as vibrações.

Por fim é feito um estudo prático de diversas microestruturas com pouca participação na literatura científica quanto à variação de índice de um líquido como quanto à variação de temperatura. As estruturas são tips com geometrias de gota, cilíndrica e cónica para além de estruturas com microesferas em série com tip. As estruturas mais longas e finas são as mais sensíveis.

Palavras-chave: Sensor em Fibra Óptica, Microesfera, Sensor de Curvatura, Cantiléver, Taper.

Contents

Acknowledgements v

Abstract vii

Resumo ix

Contents xi

List of Figures xiii

1 Introdution 1
- 1.1 Motivation . . . 1
- 1.2 Objectives . . . 3
- 1.3 Outputs . . . 4

2 Simulation and Fabrication 5
- 2.1 Microspheres and simulation of their performance . . . 5
- 2.2 Manufacturing . . . 11

3 Fiber microsphere coupled in a taper for a large curvature range 13
- 3.1 Introduction . . . 13
- 3.2 Manufacture and assembly of sensor . . . 13
- 3.3 Experimental results and discussion . . . 15
- 3.4 Conclusion . . . 20

4 Fiber micro-cantilever displacement detection 21
- 4.1 Introdution . . . 21
- 4.2 Manufacture and assembly of sensor . . . 22
- 4.3 Experimental results . . . 24
  - 4.3.1 Contact Sensor . . . 24
  - 4.3.2 Vibration sensor . . . 25
  - 4.3.3 Temperature characterization . . . 26
- 4.4 Conclusion . . . 29

5 New complex microstructures at the fiber optic end 31
- 5.1 Refractive index and low temperature sensors . . . 31
  - 5.1.1 Introdution . . . 31

5.1.2 Setup configuration . . . 32
5.1.3 Narrow tip sensor . . . 34
5.1.3.1 Experimental results . . . 35
5.1.4 Wide tip sensor . . . 37
5.1.4.1 Experimental results . . . 38
5.1.5 Dual-microsphere and tip sensor . . . 40
5.1.5.1 Experimental results . . . 41
5.1.6 Conclusion . . . 44
5.2 High temperature sensors . . . 45
5.2.1 Introduction . . . 45
5.2.2 Setup configuration . . . 45
5.2.3 Dual-microsphere, taper and tip sensor . . . 46
5.2.3.1 Experimental results . . . 48
5.2.4 Tip sensor . . . 49
5.2.5 Conclusion . . . 51

6 Conclusion **53**

A Simulation code in python **55**

Bibliography **65**

List of Figures

1.1 Mirosphere . . . 2
1.2 Cover of October's Fibers Magazine (Volume 7, Issue 10) . . . 4

2.1 Microsphere simulation: (A) frame 185 and (B) frame 390. . . . 8
2.2 Microsphere simulation with the center misaligned in relation to the fiber optic core: (A) frame 183 and (B) frame 390. . . . 8
2.3 Micro-ellipsoid simulation: (A) frame 185 and (B) frame 390. . . . 9
2.4 Curvature sensor simulation: (A) Linear power and (B) Power in dB. . . . 10
2.5 Micro-cantilever simulation: (A) Linear power and (B) Power in dB. . . . 10
2.6 Fabrication scheme: (A) micro-torch, (B) electric arc and (C) CO_2 lasers. . . . 11

3.1 Fabrication scheme. . . . 14
3.2 Experimental setup. . . . 15
3.3 Normalized output spectrum as a function of wavelength and curvature: (A) 2D and (B) 3D. . . . 16
3.4 Total power for wavelengths bands under than 1580 nm and above 1580 nm. 16
3.5 Slope of the linear adjustment as a function of the wavelength in the range: (A) $[1,3]$ (m^{-1}) and (B) $[1,5]$ (m^{-1}). . . . 17
3.6 Evolution of the transfer function with the variation of the curvature for two wavelengths: 1526.00 nm, with greater slope, and 1609.10 nm, with lower slope. . . . 17
3.7 Spectrum obtained for curvature of 0.7 km^{-1} (A) and respective FFT (B). . . . 18
3.8 Slope of the wavelenght shift linear adjustment in the range $[1,3]$ (m^{-1}) as a function of the wavelength. . . . 18
3.9 Variation of the wavelengths associated with two power extrema as a function of the curvature. . . . 19
3.10 Variation of the wavelengths associated with two power extrema as a function of the radius of curvature. . . . 19

4.1 Fabrication scheme. . . . 22
4.2 Setup schematic for temperature characterisation. . . . 23
4.3 Setup schematic for the contact mode (A) and an picture of the experimental setup (B). . . . 23
4.4 Sensor response to contact with a grid: (A) path 1 and (B) path 2. . . . 24
4.5 Sensor response to contact with an oscillating surface. . . . 25
4.6 Sensor response to temperature variation: (A) in 3D and (B) in 2D. . . . 26
4.7 Features of linear adjustment of the normalization as a function of temperature for each wavelength under study. . . . 26

4.8 Sensor response for wavelength of 1570 nm as a function of temperature and cubic fit: $a_0 = 0.16 \pm 0.02$, $a_1 = (-0.000 \pm 0.002)\,^oC^{-1}$, $a_2 = (2 \pm 5)\,10^{-5}\,^oC^{-2}$, $a_3 = (-3 \pm 4)\,10^{-7}\,^oC^{-3}$ and $r^2 = 0.992$. 27
4.9 Structure response when only the tip temperature is changed and is exposed to an oscillation of 0.2 Hz: cooling from 70 ^oC to 50 ^oC (A) and from 29.7 ^oC to 28.5 ^oC (B). 28
4.10 FFT from figure 4.9.B. 28
4.11 Structure response when approaching the aluminum plate. 29

5.1 Setup scheme for characterisation of liquid refractive index variation. 32
5.2 Calibration curve of the refractive index according to the density of dissolved sugar with a slope of $(0,137 \pm 0,004)\ R.I.U. \times \frac{ml}{g}$ and $r^2 = 0,995$. . . 33
5.3 Setup schematic for temperature characterisation. 33
5.4 Narrow tip sensor geometry. 34
5.5 Manufacturing scheme of the narrow tip sensor. 34
5.6 Output beam intensity as a function of the liquid refractive index for each wavelength: (a) in 3D and (b) in 2D. 35
5.7 Narrow tip sensor response for wavelength of 1541.78 nm and cubic fit: $a_3 = (1.4 \pm 0.1)\,10^6\ R.I.U.^{-3}$, $a_2 = (-5.6 \pm 0.6)\,10^6\ R.I.U.^{-2}$, $a_1 = (7.5 \pm 0.8)\,10^6\ R.I.U.^{-1}$, $a_0 = (-3.3 \pm 0.3)\,10^6$ and $r^2 = 0.990$. 35
5.8 Output beam intensity as a function of temperature for each wavelength: (A) in 3D and (B) in 2D. 36
5.9 Narrow tip sensor response for wavelength of 1532.84 nm and linear fit: $a_1 = (-3.51 \pm 0.06)\,10^{-5}\,^oC^{-1}$, $a_0 = (5.60 \pm 0.04)\,10^{-3}$ and $r^2 = 0.998$. 36
5.10 Relative extreme shift which, for the output spectrum related to room temperature, is 1544.10 nm and linear fit: $a_1 = (8.8 \pm 0.3)\,10^{-3}\ nm^oC^{-1}$, $a_0 = (-5 \pm 3)\,10^{-2}\ nm$ and $r^2 = 0.990$. 37
5.11 Wide tip sensor geometry. 37
5.12 Manufacturing scheme of the wide tip sensor. 38
5.13 Wide tip sensor response as a function of the liquid refractive index for each wavelength: (A) in 3D and (B) in 2D. 38
5.14 Wide tip sensor response for wavelength of 1525.00 nm and linear fit: $a_1 = (0.49 \pm 0.04)\ R.I.U.^{-1}$, $a_0 = 0.66 \pm 0.05$ and $r^2 = 0.97$. 39
5.15 Wide tip sensor response as a function of temperature for each wavelength: (A) in 3D and (B) in 2D. 39
5.16 Wide tip sensor response for wavelength of 1564.09 nm and cubic fit: $a_3 = (-1.09 \pm 0.05)\,10^{-7}\ R.I.U.^{-3}$, $a_2 = (2.2 \pm 0.1)\,10^{-5}\ R.I.U.^{-2}$, $a_1 = (-1.28 \pm 0,06)\,10^{-3}\ R.I.U.^{-1}$, $a_0 = 0.235 \pm 0.001$ and $r^2 = 0.997$. 40
5.17 Dual-microsphere and tip sensor geometry. 40
5.18 Manufacturing scheme of the dual-microsphere and tip sensor. 41
5.19 Dual-microsphere and tip sensor response as a function of the liquid refractive index for each wavelength: (a) in 3D and (b) in 2D. 42
5.20 Dual-microsphere and tip sensor response for wavelength of 1554.59 nm and cubic fit: $a_3 = (1.3 \pm 0.3)\,10^2\ R.I.U.^{-3}$, $a_2 = (-5 \pm 1)\,10^3\ R.I.U.^{-2}$, $a_1 = (7 \pm 1)\,10^3\ R.I.U.^{-1}$, $a_0 = (-3.2 \pm 0,6)\,10^3$ e $r^2 = 0.994$. 42
5.21 Output beam intensity as a function of temperature for each wavelength: (A) in 3D and (B) in 2D. 43

5.22 Dual-microsphere and tip sensor response for wavelength of 1554.45 nm and linear fit: $a_1 = -6.6 \pm 0.2\,(10^{-5}\,^{o}C^{-1})$, $a_0 = 2.33 \pm 0.02\,(10^{-2})$ e $r^2 = 0.990$. 43
5.23 Relative extreme shift which, for the output spectrum referring to the lowest refractive index, is located at wavelength 1530.57 nm and linear fit: $a_1 = (-0.020 \pm 0.001)\,nm\,^{o}C^{-1}$ e $a_0 = (0.42 \pm 0.09)\,nm$ and $r^2 = 0.97$. 44
5.24 Setup schematic for temperature variation characterisation. 46
5.25 Dual-microsphere, taper and tip sensor geometry. 46
5.26 Manufacturing scheme of the dual-microsphere, taper and tip sensor. 47
5.27 Dual-microsphere, taper and tip sensor response as a function of temperature for each wavelength: (A) in 3D and (B) in 2D. 48
5.28 Dual-microsphere, taper and tip sensor response for wavelength: (a) 1526, 90 nm and square fit: $a_2 = (-3.4 \pm 0.2)\,10^{-8}\,^{o}C^{-2}$, $a_1 = (-1.0 \pm 0.1)\,10^{3}\,^{o}C^{-1}$, $a_0 = (2.6 \pm 0.1)\,10^{3}$ and $r^2 = 0.990$; (b) 1534.24 nm and cubic fit: $a_3 = (-3.3 \pm 0.9)\,10^{-11}\,^{o}C^{-3}$, $a_2 = (3.1 \pm 0.6)\,10^{-8}\,^{o}C^{-2}$, $a_1 = -5 \pm 1\,(10^{-6}\,^{o}C^{-1})$, $a_0 = (2.80 \pm 0.05)\,10^{-5}$ e $r^2 = 0.990$. 48
5.29 Tip sensor geometry. 49
5.30 Manufacturing scheme of the tip sensor. 49
5.31 Tip sensor response as a function of temperature for each wavelength: (A) in 3D and (B) in 2D. 49
5.32 Tip sensor response for wavelength: (A) 1535.34 nm and linear fit: $a_1 = (2.38 \pm 0.07)\,10^{-6}\,^{o}C^{-1}$, $a_0 = (7.39 \pm 0.03)\,10^{-3}$ and $r^2 = 0.991$; (B) 1561.88 nm and cubic fit: $a_3 = (1.8 \pm 0,2)\,10^{-11}\,^{o}C^{-3}$, $a_2 = (-1.6 \pm 0.2)\,10^{-8}\,^{o}C^{-2}$, $a_1 = (1.3 \pm 0.5)\,10^{-6}\,^{o}C^{-1}$, $a_0 = (3.38 \pm 0.04)\,10^{-5}$ and $r^2 = 0.997$. 50
5.33 Relative extreme shift which, for the output spectrum related to the room temperature, is in the wavelength: (a) 1530.81 nm and linear fit: $a_1 = (1.20 \pm 0.04)\,10^{-2}\,nm^{o}C^{-1}$, $a_0 = (-1.2 \pm 0.1)\,nm$ and $r^2 = 0.992$; (b) 1553.02 nm and square fit: $a_2 = (1.7 \pm 0.2)\,10^{-5}\,nm^{o}C^{-1}$, $a_1 = (5 \pm 1)\,10^{-3}\,nm^{o}C^{-1}$, $a_0 = (-0.08 \pm 0.1)\,nm$ and $r^2 = 0.997$. 50

Chapter 1

Introdution

1.1 Motivation

Measurement is the science of control. Since the beginning of civilization there has been a concern to develop precise ways to quantify various dimensions for agricultural, construction and trade purposes. Later, with the industrial revolution, the machines appeared. Some with the purpose of production and others with the purpose of gauging the state of certain systems in order to allow the correct performance as well as the determination of anomalies. The latter are designated as sensors [1]. With the advancements of electronics at the beginning of the 20th century, electronic sensors dominate this century and began with the invention of the first temperature controller, the Warren Johson thermostat. However, since the 1960s, there have been great developments in the field of optics such as lasers [2] and waveguides such as fiber optics [3]. Thus the metallic coaxial cables began to be subsisted by optical fiber and verified that the optical systems besides of being insensitive to electromagnetic fields and reveal more precision in the measurements than the electronic sensors. Thus, today there is a run for the development of optical systems not only as sensors [4] but also for processing [5–7] since the working bandwidth is much higher than the corresponding electronic systems.

Today, optical sensors are divided into three main sectors: interferometric sensors [8], intensity sensors [9] and sensors with wavelength measurement [10]. Interferometric sensors create two or more optical paths based on the input beam and combine them to create constructive and destructive interference zones (interference patterns). Thus, the output spectrum contains several fringes whose characteristics allow to evaluate the physical

quantity in measurement. The intensity sensors are those that change the beam light intensity. This can be achieved by light dispersion, photo-emission or photo-absorption, or by changing the transmissivity of the optical medium. Wavelength sensors consist of measuring the deviation of the spectrum extremes. In this type of sensors, interferometric sensors can also be included in addition to nonlinear sensors.

An area with strong study in recent years is the resonant microstructures. The most studied geometries are: torus [11], disk [12], capillary [13] (or cylindrical structures) and microspheres [14] (figure 1.1). In all of them, the operation consists in the excitation of circular modes and the beam is coupled to these structures by means of evanescent wave. Another common characteristic is the fact that they present quality factors equal or superior to 10^5 [15] with the exception of the microsphere which is superior to 10^9 [16]. The main reason is that the surface imperfections are very small. It should be noted that the highest value of the Q factor is in the microspheres due to the modes being strongly confined. One of the great advantages of these structures is the fact that the beam overlaps, resulting in interference patterns and the appearance of nonlinears even with low-power and low-coherence beams. But, given the difficulty of implementing these systems due to the strong sensitivity to vibrations as well as to impurities contained on the surface, these structures are unusual as sensor.

However, there are methods of manufacturing where the microspheres [17] have a rod allowing excitation without being influenced by vibrations. But as mentioned in the previous paragraph, the beam that propagates inside is strongly confined, being the problem for some cases. For others, is exceptional because allows the beam to disperse without suffering transitions between different refractive index media. Furthermore, it can be said

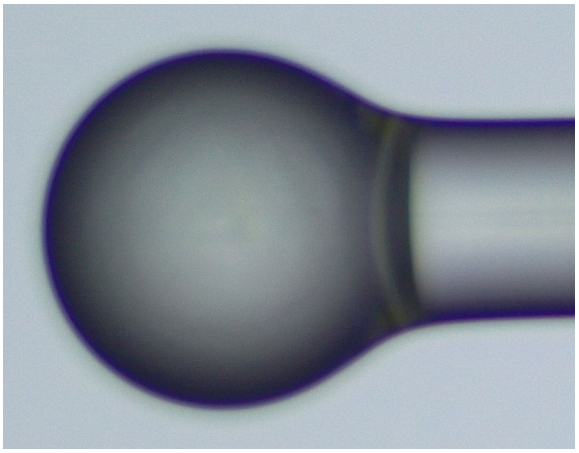


FIGURE 1.1: Mirosphere

that the opposite of microspheres are the tips [18]. These structures are similar to cones and allow to reduce the size of the beam. In addition, it reduces the confinement, which leads to a greater interaction with the the external environment.

In chapter 2 there is an analysis of the microsphere performance as well as the sensors of chapter 3 and 4 by means of simulations based on the "Symmetric Split Fourier" method. In addition, the fabrication of the microsphere is presented as well as the physical characterization.

Chapter 3 describes the manufacture of the curvature sensor as well as its characterization. This sensor is interferometric and has two reading modes: in intensity and in spectrum's variation

Chapter 4 describes the manufacture of the micro-cantilever. In addition, is proven that there are two operating modes: in reflection (the main feature is the safeguard of the sensor head) and in contact (allows greater accuracy). In addition, allows to determine the characteristics of the mechanical waves that propagate in a given object and has low sensitivity to temperature.

Chapter 5 presents some structures that still do not have great impact on research. Contains the fabrication as well as the characterization of these regarding the variation of the index of a liquid as well as regarding the variation of temperature.

1.2 Objectives

The objective of this work is to study the potentiality of the microsphere as well as the combination of microsphere with tips in order to allow or improve the performance as a sensor. Thus, this work fulfills the following points:

- Manufacture of complex microspheres and microstructures using the conventional splice machine;
- Develop a curvature sensor and its characterization;
- Develop a fiber optic cantilever with the capability of contact sensor, vibration sensor and proximity sensor;
- Characterization of new complex micro-structures in optical fiber for refractive index and temperature.

1.3 Outputs

- Paulo Robalinho, Orlando Frazão, "Fiber microsphere coupled in a taper for a large curvature range", Fibers, 2019, vol. 7, iss. 10, no. 87, doi: https://doi.org/10.3390/fib7100087 and is the cover of the October magazine (Volume 7, Issue 10) that is in the figure 1.2;
- Paulo Robalinho, Orlando Frazão, "Fiber micro-cantilever displacement detection", 3^{rd} Doctoral Congress in Engineering, Porto, Portugal, 2019;
- Paulo Robalinho, Orlando Frazão, "Micro-cantilever displacement detection based in optical fiber", Sensors, 2019, vol. 19, iss. 22, no. 4826, doi: https://doi.org/10.3390/s19224826.

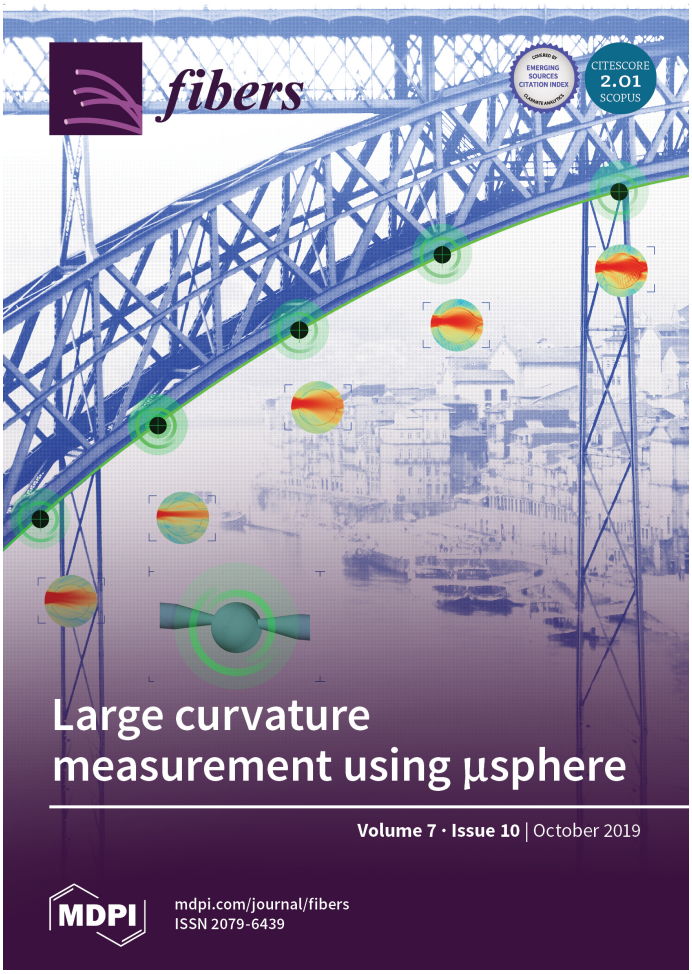


FIGURE 1.2: Cover of October's Fibers Magazine (Volume 7, Issue 10)

Chapter 2

Simulation and Fabrication

2.1 Microspheres and simulation of their performance

In the past, the dispersion was seen with something negative due to the loss of optical signal power. However, with the emergence of resonant microcavity, the dispersion became an important phenomenon in the development of new sensors as well as in the processing of optical signals . Moreover, the conception of microlasers with a large spectral band is allowed when these structures are doped with rare earths. [19, 20].

Microspheres are characterized as dielectric spherical structures. In this work, given that the beam enters in the microsphere through the rod, then the beam will disperse. The existence of several optical paths, leading to the creation of guided modes, is allowed due to the low material absorption and the possibility of reduced losses in the glass-air reflection (with total internal reflection). In this case, the dispersion results from changes in the dimensions of the medium in which the beam propagates. Thus, the optical signal obtained contains several interferences which results in the emergence of fringes in the output signal spectrum. Thus, if there is a change in the microsphere features such as: the dimensions, the external index or even the position of input and output fiber optics, causes a change in the output signal, so is a sensor. However, since the beam is strongly confined, then the influence of the external environment on the beam can be reduced.

This chapter is intended to study the microsphere performance based on simulations. The code (see appendix A) was made in python and was used the "Symmetric Split-step Fourier" method [21, 22]. These simulations are based on Schrödinger's time-dependent equation:

$$\frac{d}{dt}\Psi(t) = -i\hat{H}\Psi(t) \tag{2.1}$$

So, for the instant $t + \Delta t$,

$$\Psi(t + \Delta t) = e^{-iA}\Psi(t) \tag{2.2}$$

with $A = \int_t^{t+\Delta t} H'(t')\, dt'$. Thus the time evolution operator is

$$\hat{U} = e^{-iA} \tag{2.3}$$

In this simulation, it was considered the Hamiltonian below since the light beam power to be used in the experimental part is lower than that required to produce non-linear effects.

$$\hat{H} = \frac{1}{2}\hat{p}^2 + V(r) \tag{2.4}$$

Since

$$e^{\hat{B}+\hat{C}} = e^{\hat{B}}e^{\hat{C}}e^{\left[\hat{B},\hat{C}\right]} = e^{\hat{B}}e^{\hat{C}} \tag{2.5}$$

if $\hat{B}$ and $\hat{C}$ commute. Considering that

$$A = \int_t^{t+\Delta t} H'\left(t'\right) dt' \approx H\left(t^n\right)\, dt \tag{2.6}$$

for small dt and, consequently,

$$\hat{U} = e^{-iH(t^n)dt} = e^{-idt\frac{\hat{p}^2}{2}}e^{-idtV} \tag{2.7}$$

However, to calculate the exponential of a matrix, should be diagonal. Taking into account the Hamiltonean chosen, the term $\frac{1}{2}\hat{p}^2$ is a diagonal matrix in reciprocal space and the term $V(r)$ is represented by a diagonal matrix in direct space. So, the "Symmetric Split-step Fourier" method consists of rewriting the Hamiltonean as a sum of two operators such that

$$\hat{H} = \hat{L} + \hat{N} \tag{2.8}$$

where $\hat{L}$ is diagonal in reciprocal space and $\hat{N}$ is diagonal in direct space. In this case $TF\left[\hat{L}\right] = TF\left[\frac{1}{2}\hat{p}^2\right] = -\frac{\vec{K}^2}{2}$, where $\vec{K}$ is the wave vector, and $\hat{L} = V(r)$. So, the "Symmetric Split-step Fourier" method consist

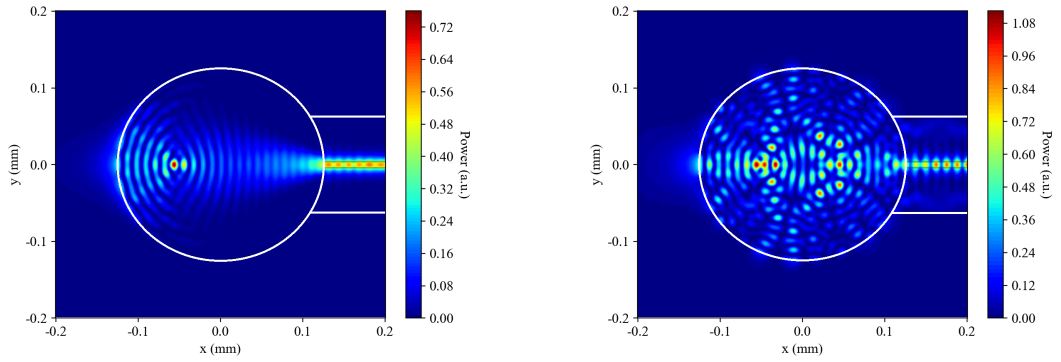
$$\Psi(t + \Delta t) = e^{-i\frac{Ldt}{2}} e^{-iNdt} e^{-i\frac{Ldt}{2}} \Psi(t) \tag{2.9}$$

Therefore, the initial state is $\Psi\left(t^0\right)$. Then, the Fourier Transform of the initial state is calculated and multiplied by the term $e^{-i\frac{Ldt}{2}}$. Then, the matrix obtained is passed into direct space and multiplied by the term e^{-iNdt}. The Fourier Transform is again calculated, but is now multiplied by the term e^{-iLdt}. This last two steps is repeated cyclically until the desired solution is obtained. The last step is to pass the matrix from direct to reciprocal space, multiply it by the term $e^{-i\frac{Ldt}{2}}$ and then move it to direct space. This matrix is $\Psi(t + \Delta t)$.

Throughout these simulations, two types of potential were used. If the system is a solid of revolution, the potential is constant by regions: the microsphere has a potential equal to the optical fiber core potencial, the cladding potential is higher than the core potential and the surrounding potential is null and the highest of the three. If the system is not a solid of revolution, the potential of the microsphere has a constant component equal to the maximum core potential and a spherical component with a tenth of the previous potential, the core and cladding have a cylindrical potential and the surrounding environment maintains the null potential.

Thus, the simulations begin by investigating what happens to a beam that arrives the microsphere through the rod (figure 2.1).

As can be seen from figure 2.1.A, the first reflection occurs at the microsphere's entry. Then, the beam is dispersed. When arrives at the glass-air interface, causes a transmission and a reflection. Although the transmission is not clearly visible due to the dispersion of the beam, is the most energetic. The beam resulting from the reflection consists of curved constant phase planes. Thus, the beam focuses and then disperse again. When arrives the rod, one part is transmitted to the fiber optic core, another to the cladding (which is absorbed by the protection) and another is reflected back into the microsphere. In addition, there are total internal reflections. These mainly occur, at an early stage, in microsphere surface. This phenomenon is responsible for the formation of circular modes. Thus, the existing modes can be divided into two types: longitudinal and circular. The longitudinal modes are characterized by containing more energy, occupying the central



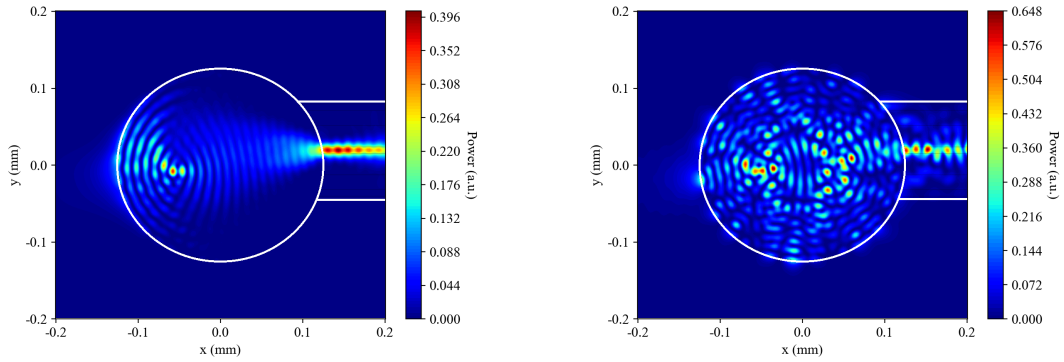
(A) (B)

FIGURE 2.1: Microsphere simulation: (A) frame 185 and (B) frame 390.

region of the microsphere and are aligned with the optical fiber core. Circular modes have less energy than longitudinal modes, are in the region near the surface of the microsphere and there is a low coupling index for the optical fiber. In the stationery solution (figure 2.1.B), it is possible to observe that the beam is strongly confined as well as there is a large loss of energy through the surface of the microsphere.

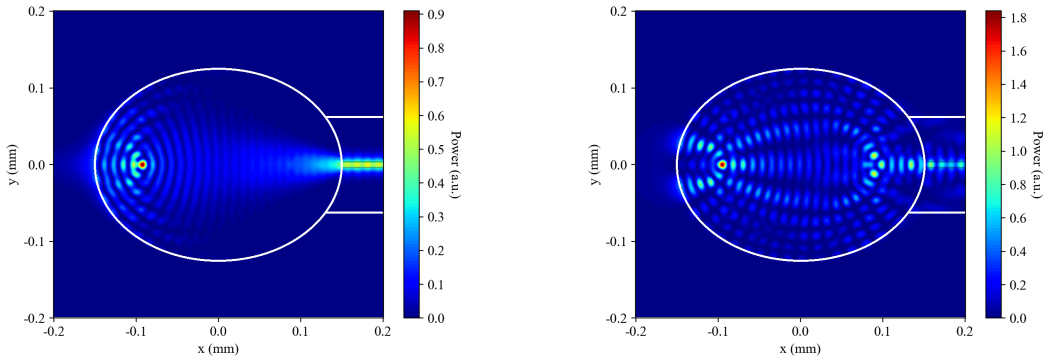
Two important features of the previous simulation is the fact that the centre of the microsphere is on the fiber optic axis and is perfectly spherical. In practice, these two conditions are not always guaranteed. Thus result the fig. 2.2 and fig 2.3. The first situation is due to the fact that gravity displaces the microsphere while is in fusion and the second situation is due to the fact that the energy is lower than that required for the structure to take the spherical shape.

The figure 2.2 corresponds to what happens if the microsphere is misaligned with the



(A) (B)

FIGURE 2.2: Microsphere simulation with the center misaligned in relation to the fiber optic core: (A) frame 183 and (B) frame 390.



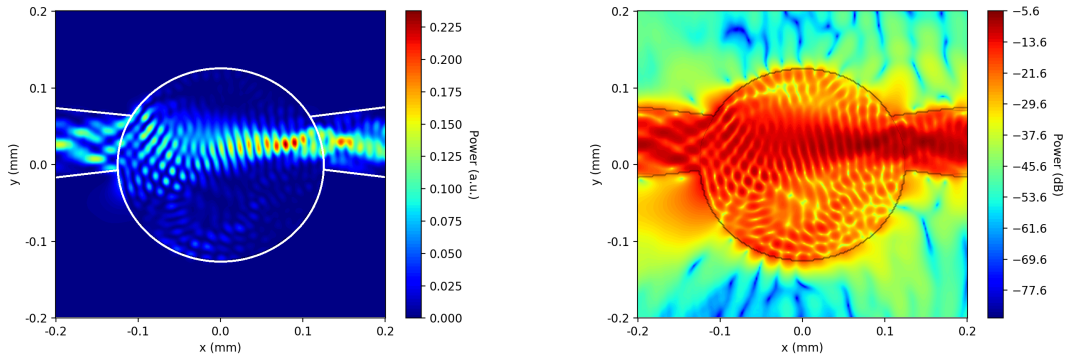
(A) (B)

FIGURE 2.3: Micro-ellipsoid simulation: (A) frame 185 and (B) frame 390.

fiber optic axis. The main difference is that the dispersion of the beam at the optical fiber exit is asymmetric. Thus, the longitudinal modes are misaligned with the core but are aligned along an oscillating line that connects the center of the fiber optic to the microsphere entrance, the center of the microsphere and the point of interception between the straight line formed by this last two points and the surface of the sphere. In addition, on the spherical surface of the opposite side of the rod, the absolute maximum is shifted from the center at the same distance as the optical fiber core is shifted in relation to the horizontal line that passes through the center of the microsphere and is parallel to the fiber optics. The last consequence is that the circular modes have more energy due to the location and direction of the beam introduction increase the presence of total internal reflection.

The figure 2.3 corresponds to the fact that the microstructure is ellipsoidal. As can be seen, the focal length decreases and the longitudinal modes located in the center of the microsphere are elongated. The loss of energy in the top and bottom of the microsphere is smaller, which leads to more energy contained in the circular modes.

As previously mentioned, one of the microsphere feature is the dispersion. Thus emerged the idea of coupling a microsphere between two fiber optics. The operation consists of varying the directionality of the beam at the input and output of the microsphere. In this case, the microsphere was placed in the middle of a taper to increase the sensitivity to fiber optic curvature. Thus results the figure 2.4. As it can be seen, the dispersion is asymmetrical in relation to the optical fiber core. Thus, the part of the beam that is coupled to the output fiber optic is spatially oscillating relative to the output optical fiber axis. Thus, if the bottom of the microsphere is illuminated, the circular modes will have a greater impact on the output spectrum and if the top of the microsphere is illuminated,

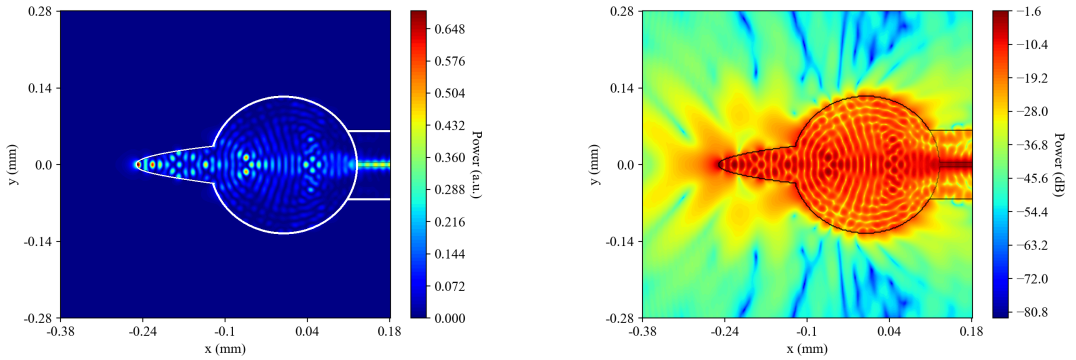


(A) (B)

FIGURE 2.4: Curvature sensor simulation: (A) Linear power and (B) Power in dB.

the longitudinal modes will have a greater impact on the output spectrum.

The sensor that is described chapter 4 (figure 2.5) consists of a microsphere to which has been fused a tip. This tip is aligned with the optical fiber core. In this case, the tip used for the simulation has the typical geometry that is obtained when is manufactured with an electric arc. As can be seen, there are three important reflections: at the entry of the microsphere, at the glass-air boundary of the microsphere and at the glass-air boundary of the tip. The dispersion of the beam caused by the microsphere will accentuate the multimode feature of the tip. In the tip there is a maximum where one part is inside the fiber tip and the other is outside the fiber tip, as can be seen in figure 2.5.b.



(A) (B)

FIGURE 2.5: Micro-cantilever simulation: (A) Linear power and (B) Power in dB.

2.2 Manufacturing

The production of microspheres can be done using [17, 23–26]:

- gas flame or micro-torch: is the oldest technique used to produce solid optical microspheres [23] (figure 2.6.A);
- electric arc: the glass fuses by means of an electric discharge, this technique is generally used with fiber splice equipment [17] (figure 2.6.B);
- CO_2 lasers: The laser beam may result in fusion of the fibre or ablation of specific parts of the intended structure [24–26] (figure 2.6.C).

All of them consist of heating a optical fiber tip which, during the fusion process, experiences a change of geometry in the fiber tip due to surface tensions. The new geometry is spherical with a diameter greater than the initial optical fiber diameter. This last fact leads to take into account the direction of the fiber optic in relation to the gravity field since the heating makes the optical fiber more ductile and, given the increased weight of the end throughout the process, the rod (optical fiber) tends to bend.

Gas flame fabrication was used at the beginning of the study of microspheres at the end of the 20th century. However, due to the difficulty in stabilizing the flame, with variations in heat flow, as well as the introduction of unwanted doping, this technique was abandoned.

Nowadays, the most used techniques are the last two mentioned above. In both techniques is possible to fabricate microspheres with a diameter higher than the fiber or through a glass powder or a portion of glass. Although the existing manufacturing

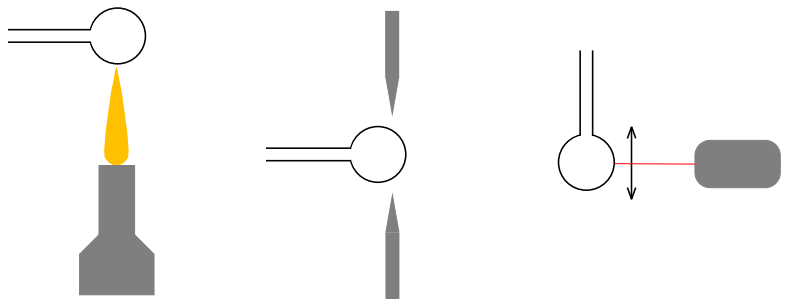


FIGURE 2.6: Fabrication scheme: (A) micro-torch, (B) electric arc and (C) CO_2 lasers.

descriptions show significant differences in the use of the two techniques, the procedure is the same. The main differences are:

- implementing a laser system with focusing lenses (especially in the IR region) is more expensive and requires more complex calibration than an electric arc system;
- the use of the laser allows the precise definition of the heating or ablation location of the optical fiber (contrary to the electric arc that only allows heating the entire optical fiber tip), making the manufacture of microcavity more easy.

However, in the following work, it is demonstrated that, despite the greater complexity in the production of microstructures at the optical fiber tip using an electric arc, this allows not only the conception of microstructures but also the geometry quality is similar if they were produced using a CO_2 laser. In addition, since the electric arc heats the entire structure, then the structures have greater mechanical robustness than the structures produced by laser.

Chapter 3

Fiber microsphere coupled in a taper for a large curvature range

3.1 Introduction

Nowadays, microspheres have been used as sensor elements such as temperature, deformation and others. In addition, tapers are also used as sensor elements of refractive index, curvature, among others.

This chapter contains the study of a new structure that consists of the combination of the two structures listed in the previous paragraph, this is, a microsphere fused between a taper. In this work, it is demonstrated the capability of this structure as a curvature sensor. The microsphere has a diameter of 258 μm. The taper increases the sensitivity of beam dispersion within the microsphere which allows for an increase in the quality of the measurement of the curvature to which the fibers are subjected, either as a function of power variation or as a function of the relative extrema of the spectrum.

3.2 Manufacture and assembly of sensor

The system is made from standard single-mode fiber and consists of a microsphere that has been fused in the middle of a taper where the taper is misaligned with the center of the microsphere (figure 3.1). Follows the manufacturing process:

- microsphere (apply an electric arc for 5 s so that surface roughness is minimal, for this the "Sumitomo Eletric Type-72C" splice machine was used in the manual mode and with a power of 100 $u.a.$);

- Taper (figure 3.1.A) (produce the narrowing at the end of two fibers by splice between two fibers with an arc equal to or greater than 20 s and and intensity of 50 u.a., at the same time, stretch the fibers by varying the point of arc's application);
- Cleave the taper;
- Fuse the microsphere with the end of a taper (figure 3.1.B) (make the connection between the microsphere and the narrowed fibers with an intensity's electric arc of 20 $u.a.$ and duration of 1 s);
- Clamp the stem of the microsphere (figure 3.1.C);
- Fusion between the microsphere and the other taper (figure 3.1.D).

The interrogation system used to read the microsphere was an Optical Spectrum Analyzer (OSA) "Advantest Q8384" with a resolution of 0.02 nm and a wide spectrum source in the 1550 nm region with a width of 100 nm. See figure 3.2:

The fiber was stretched between two supports that are distant 2.825 m and one of the holder contains a micrometer translation stage. By varying this translation stage, allows to vary the curvature of the fiber that following the expression [27]

$$\left(\frac{1}{R}\right) = \frac{2d}{(d^2 + l^2)} \tag{3.1}$$

where l the half distance between supports and d is the flexion displacement. Microsphere placement occur before connecting the fibers to both the source and the OSA and is located on the outside of the bend.

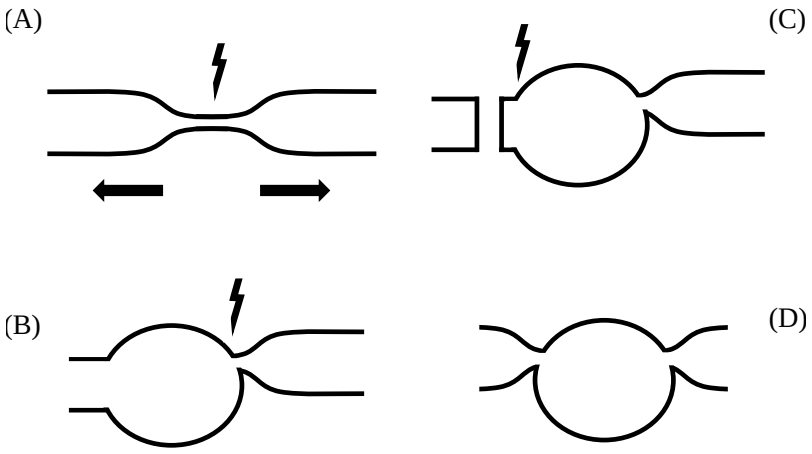


FIGURE 3.1: Fabrication scheme.

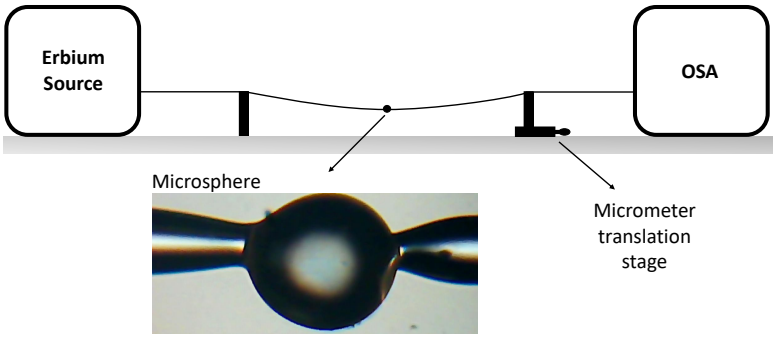


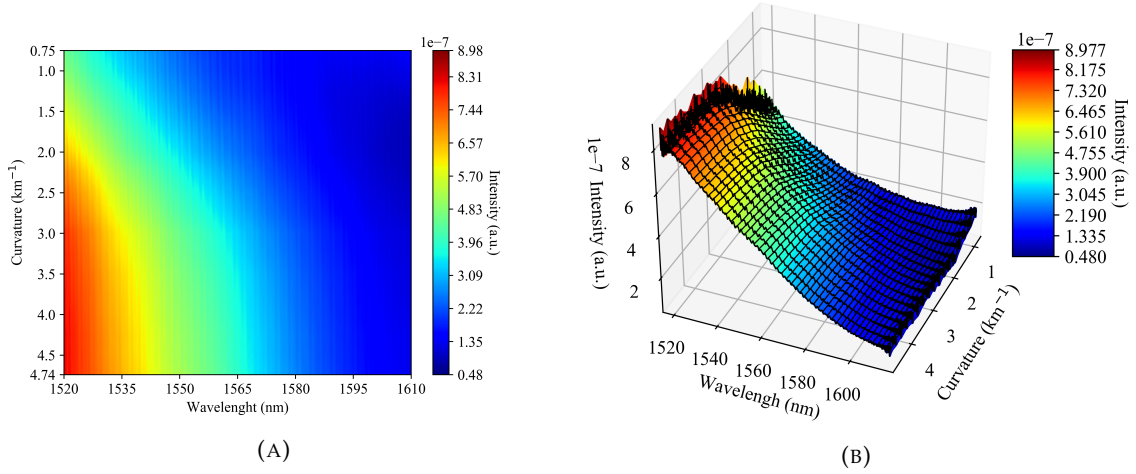
FIGURE 3.2: Experimental setup.

The implementation of the taper reduces the light intake cone and, the narrower is, the greater the visibility associated with interference fringes but output power is lower. These interferences are differ if the microsphere is placed inside or outside the curvature due to geometry asymmetry (figure 3.2). If the microsphere is placed outside the curvature, the output signal exhibits a greater impact from multiple interferences. If the microsphere is positioned inside the curve, this will only be a power sensor due to fibers misalignment and the output spectrum contains more power. In addition, if the microsphere is larger, the difference between optical paths increases but the output signal intensity will be lower. This is due to the increase of beam dispersion as well as the increase of reflections. If the microsphere is smaller, the length of the optical paths will be shorter and the difference between them will be small.

3.3 Experimental results and discussion

From the characterization of the sensor as a function of curvatures, result the graphs of figure 3.3. There are several fringes that are related to the interference of various optical pathways where it follows that the profile of low curvature intensity differs from the profile associated with larger curvatures.

In figure 3.4, for wavelengths higher than $1580\,nm$, for the interval of $[1,3]\,(km^{-1})$, the slope is $(6.8 \pm 0.1) \times 10^{-6}\,km$ with a r^2 of 0.994 and, for the interval of $[3,5]\,(km^{-1})$, the slope is $(1.4 \pm 0.1) \times 10^{-6}\,km$ with a r^2 of 0.990. For wavelengths lower than $1580\,nm$, for the entire range of curvatures under study, the slope is $(7.0 \pm 0.5) \times 10^{-7}\,km$ with a $r^2 = 0.94$.



(A) (B)

FIGURE 3.3: Normalized output spectrum as a function of wavelength and curvature: (A) 2D and (B) 3D.

For the study of sensor's sensitivity with respect to the power variation, result the graphs of figure 3.5 which contain the slope of the linear fit for each wavelength referring to the curvature interval $[1,3]\ (km^{-1})$ (figure 3.5.A) and $[1,5]\ (km^{-1})$ (figure 3.5.B). The results can be divided into two components, a linear and a oscillatory. The linear component results from the narrowing of the input and output fiber and the oscillatory component results from the interference of the optical paths. Thus is determined that the wavelength where the maximum sensitivity occurs is 1526.00 nm in the range of $[1,3]\ (km^{-1})$. The minimum sensitivity occurs at 1609.10 nm in the range of $[1,5]\ (km^{-1})$. Regarding the study of linearity, for wavelength 1526.00 nm, for the interval of $[1,3]\ (m^{-1})$ the slope is $(1.77 \pm 0,03) \times 10^{-7}\ km$ with a r^2 of 0.990 and for the interval of $[3,5]\ (m^{-1})$ the slope is $(1.5 \pm 0.2) \times 10^{-8}\ km$ with a r^2 of 0.95, and for wavelength 1609.10 nm, for the entire range

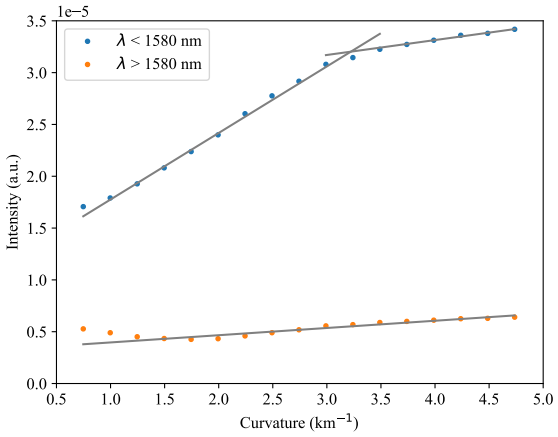


FIGURE 3.4: Total power for wavelengths bands under than 1580 nm and above 1580 nm.

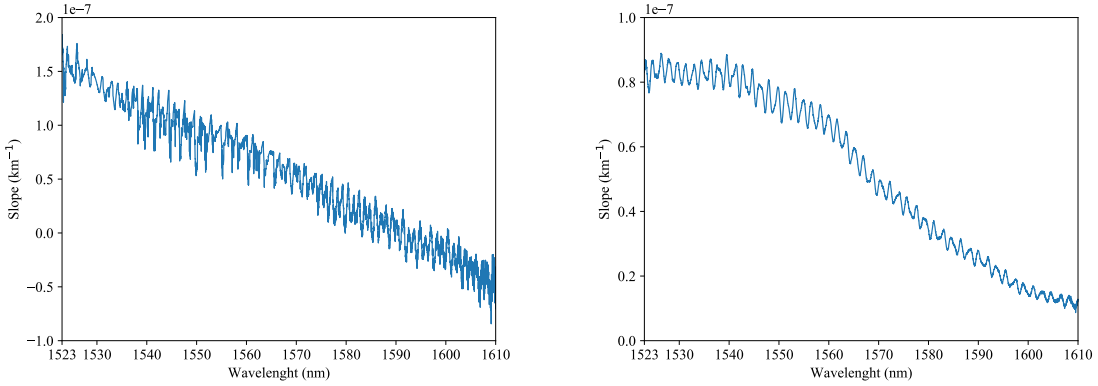


FIGURE 3.5: Slope of the linear adjustment as a function of the wavelength in the range: (A) $[1,3]\ (m^{-1})$ and (B) $[1,5]\ (m^{-1})$.

of study curvatures, the slope is $(3 \pm 3) \times 10^{-9}\, km$.

The FFT (Fast Fourier Transform) has been calculated and demonstrates the existence of three main interferometers (figure 3.7). In addition, the wavelength variations where the relative extremums of the spectrum are located are a result of the phase variation introduced by the optical system under study. Optical pathways result from beam dispersion within the microsphere and the fact that the microsphere creates two mirrors, one at the top and one at the bottom. As geometry is asymmetric, then exist the generation of three interferences: two between the signal that moves in a straight line between the tapers and the light reflected in the mirrors and a third interference between the reflected light in the two mirrors.

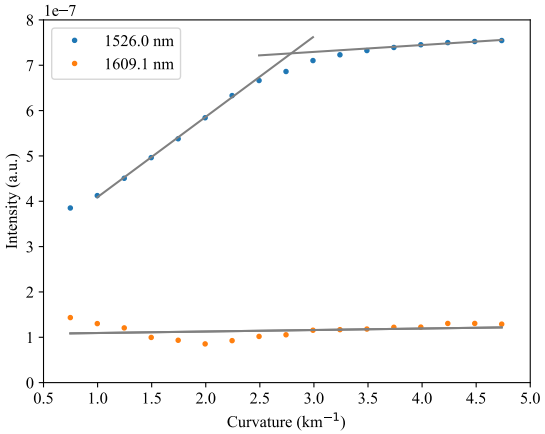
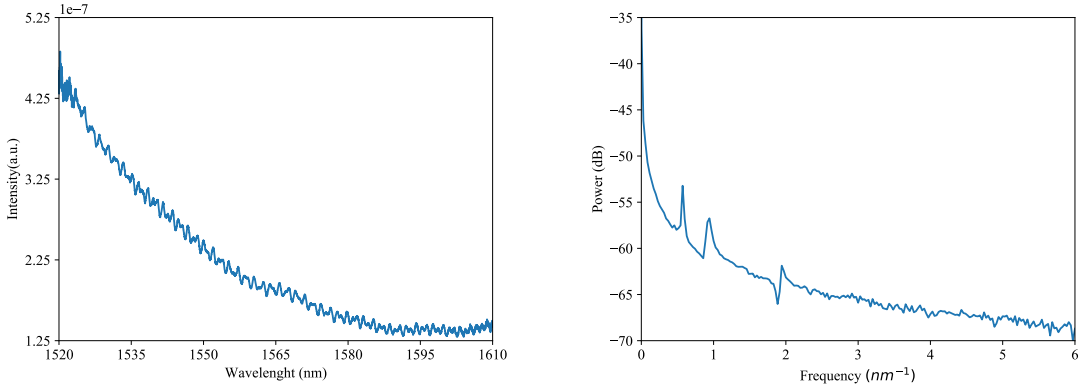


FIGURE 3.6: Evolution of the transfer function with the variation of the curvature for two wavelengths: 1526.00 nm, with greater slope, and 1609.10 nm, with lower slope.



(A) (B)

FIGURE 3.7: Spectrum obtained for curvature of $0.7\,km^{-1}$ (A) and respective FFT (B).

The maxima and minima, as the curvature increases, move to larger wavelengths. In the figure 3.8 contains the slope for several relative extremes for the linear fit corresponding to the range of curvatures $[1,3]\ (km^{-1})$. The wavelengths in the $1600\,nm$ region are more sensibility than wavelenghs in the $1520\,nm$ region. Thus, the maximum sensitivity is at $1594.88\,nm$ and the minimum sensitivity is at $1525.34\,nm$.

Regarding the linearity study, figure 3.9, for wavelength $1594.88\,nm$, for the interval of $[1,3]\ (km^{-1})$ the slope, in module, is $(580 \pm 20)\ pm \cdot km$ with a r^2 of 0.990 and for the interval of $[3,5]\ (m^{-1})$ the slope, in module, is $(230 \pm 30)\ pm \cdot km$ with a r^2 of 0.93, and for wavelength $1525.34\,nm$, for the interval of $[1,3]\ (m^{-1})$ the slope in modulo is $(410 \pm 20)\ pm \cdot km$ with a r^2 of 0.98 and for the interval of $[3,5]\ (m^{-1})$ the slope in module is $(80 \pm 8)\ pm \cdot km$ with a r^2 of 0.95. The figure 3.9 contains the same wavelenght range

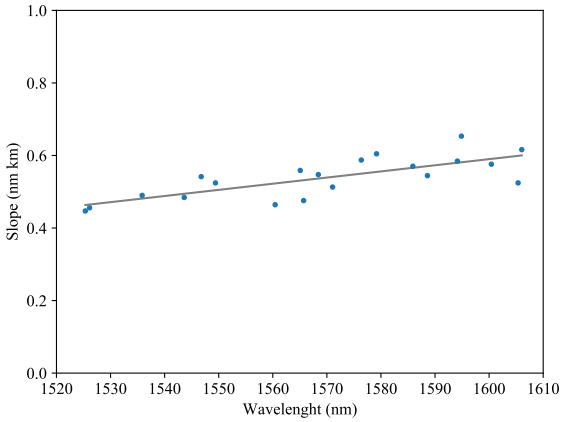
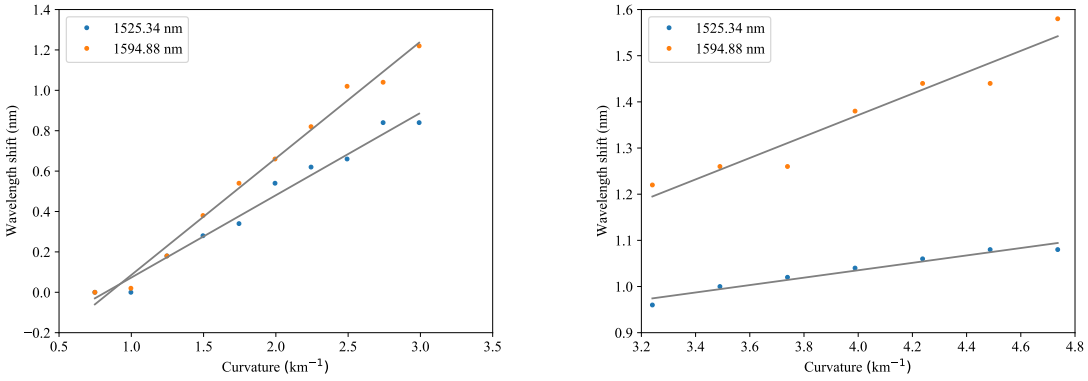


FIGURE 3.8: Slope of the wavelenght shift linear adjustment in the range $[1,3]\ (m^{-1})$ as a function of the wavelength.



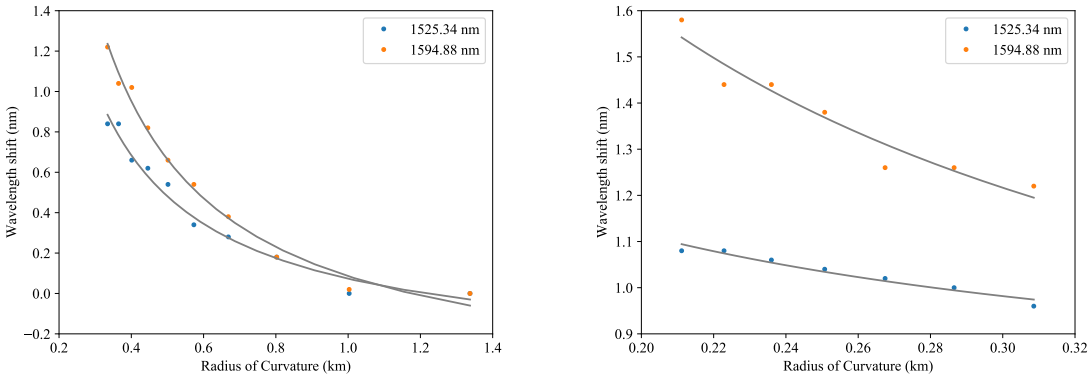
(A) (B)

FIGURE 3.9: Variation of the wavelengths associated with two power extrema as a function of the curvature.

as that of figure 3.10 but depending on the radius of curvature.

The existence of both regions is due to the elasticity of the taper. This is, when the sensor is subjected to a lower curvature than $3\,km^{-1}$, the taper follows this curvature and strongly influences the optical paths. For curvatures higher than $3\,km^{-1}$, the taper does not acquire the expected curvature to which the system is subjected and a loss of sensitivity occurs. Thus, given that the maximums of the spectrum can be obtained with the equation $m = \frac{2nl}{\lambda}$, for curvatures lower than $3\,km^{-1}$, the wavelengths associated with the extremes of the spectrum increase, so the length of the optical path also increases. For curvatures higher than $3\,km^{-1}$, as the wavelength stabilizes then the optical path length also stabilizes.

Throughout the practical work, the entire structure demonstrated a good resistance to



(A) (B)

FIGURE 3.10: Variation of the wavelengths associated with two power extrema as a function of the radius of curvature.

mechanical stresses in addition to having been observed variations of signal due to these tensions.

3.4 Conclusion

Thus, when the curvature of the system, microsphere plus narrowed fibers, it is changed gives rise to variations of several optical pathways that are associated to interferences. This will change the output signal power. For sensor based on power's variation, is also proven the existence of a region with a linearity between $1\,km^{-1}$ and $3\,km^{-1}$ whose sensitivity is higher for wavelengths located at $1526.00\,nm$. In addition, as the curvature increases there are linear phase variations. This results in local variations of the relative extremums of the output spectrum for the same range mentioned above. In this case the sensitivity is maximum for wavelengths at $1594.88\,nm$.

This work prove that this type of geometry allows to accurately measure large curvatures which the fiber is subjected, opening the door for its application not only as a sensor of curvature but also of oscillations. To reduce reflection losses, a coating can be used to increase the internal reflectivity, however, the mobility of the input and output fibers must be taken into account. This structure can be implemented as a curvature sensor for large structures such as bridges, tunnels and buildings.

Chapter 4

Fiber micro-cantilever displacement detection

4.1 Introdution

The AFM (Atomic Force Microcopy) is one of the most important technique in the characterization of micro and nano structures [28]. This technique uses a cantilever, a metal tip that reflects a laser beam. Thus, as the cantilever travels through a given surface, there is a variation in the light beam position in the optical sensor, allowing the profile of a given surface to be determined. However, given the complexity of cantilever production as well as fragility, the AFM is associated with a high cost. Furthermore, does not allow characterization of micro and nano processes as well as elaborate structures due to the low speed of image acquisition [29] and there is a possibility of scratching soft materials.

Since fiber optics structures have shown good results as sensors, they are also candidates for replacing AFM metalic cantilever [30]. The most commonly used structures are: conical geometries in reflection mode [31–33] and, in contact mode, structures similar to current cantilevers that are fuse to a cleaved fiber whose production is complex [34].

This chapter describes the fabrication of a structure at the fiber end in order to replace the cantilevers, increase the sensitivity and decrease the complexity that consequently reduces the manufacturing costs. The geometry presented here consists of a microsphere with a diameter of 165 μm and a fiber tip with a length of 82 μm, a width of 38 μm in the wider region and 13 μm in the thinner zone. The fiber tip is aligned with the core of the microsphere rod. The beam dispersion caused by the microsphere is low and the fact

that the junction region of tip and microsphere is 38 μm, the optical pathways are mostly influenced by tip. The microsphere emerges as a byproduct of the fusion of tip to fiber.

4.2 Manufacture and assembly of sensor

The geometry under study consists of a tip and a microsphere that is a byproduct of tip fabrication. The entire structure consists of standard fiber and the "Sumitomo Electric Type-72C" splice machine was used. The manufacture follows the next steps:

- Make a tip: produce a taper (splice between two fibers with an arc duration of 10 s and a power of -40 $u.a.$, and at the same time stretch the fibers by varying the point of application of the arc) - to form two tips, should apply a tension that leads to the taper split (figure 4.1 (A) and (B));
- Formation of the structure: fuse a cleaved fiber to the tip (with the same power and duration shown in the previous point, but the electric arc is applied to the tip stem and apply a tension that leads to the separation of the tip from the stem). Thus occurs the formation of a narrower tip than the tips formed in the previous point and without the existence of a taper cone between this and the stem. One consequence is the formation of a microsphere between the fiber and the tip that does not influence the performance of the structure as a contact sensor (figure 4.1 (C) and (D)).

The interrogation system used to characterize the system was an Optical Spectrum Analyzer (OSA), "Advantest Q8384", with a resolution of 0.02 nm and a broad spectrum source in the region of 1570 nm with a width of 100 nm.

In this work is studied the sensitivity on contact with a surface as well as the variation of the output signal as a function of temperature. For this two assembly schemes were

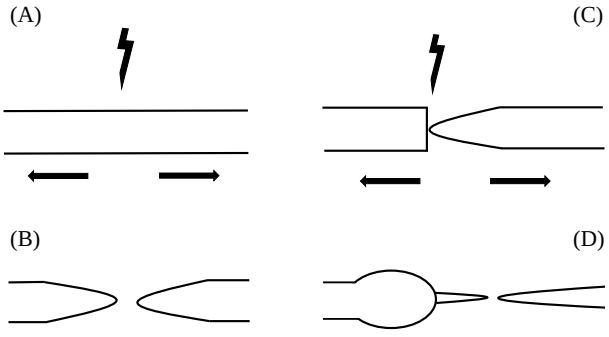


FIGURE 4.1: Fabrication scheme.

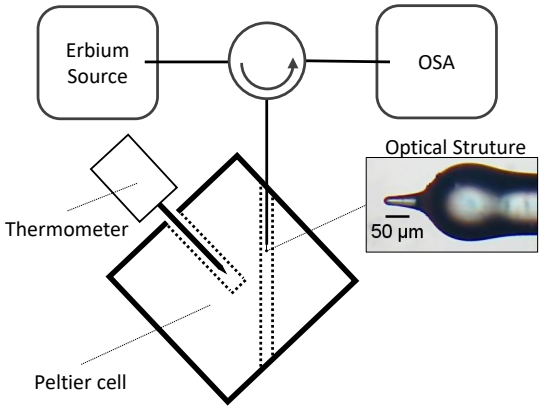
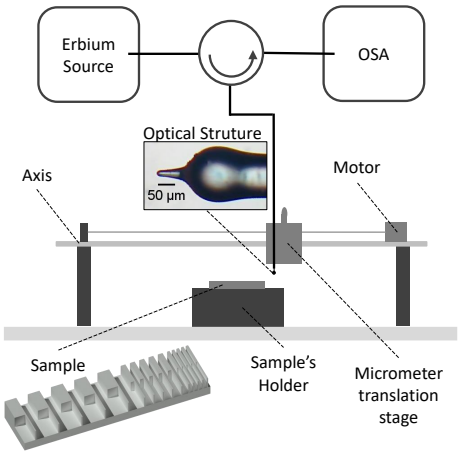


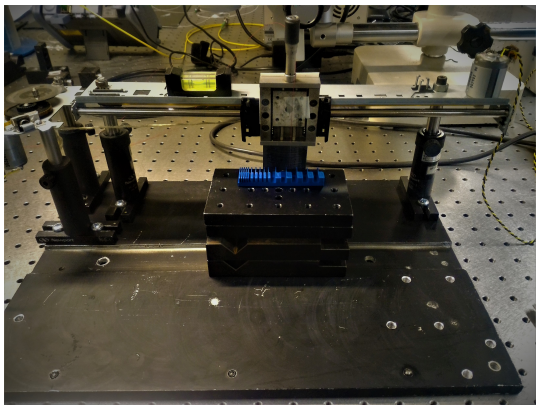
FIGURE 4.2: Setup schematic for temperature characterisation.

used. In the scheme of figure 4.2, the structure is placed inside a metal plate which is heated using a peltier element cell. In the scheme of figure 4.3, the fiber is placed in a micrometer translation support, which is attached to a carriage.

The displacement is controlled by DC motor allowing to scan a grid in a given direction. The grid is composed of two path whose characteristics are presented in the table 4.2. Grid profile characterization begins with the sensor surrounded only by the air. The grid was kept at a constant temperature and static.



(A)



(B)

FIGURE 4.3: Setup schematic for the contact mode (A) and an picture of the experimental setup (B).

TABLE 4.1: Grid Properties: this consists of two paths that has square profiles.

Period		Elevation dimension (Path 1)		Elevation dimension (Path 2)	
#	Length (mm)	Length (mm)	height (mm)	Length (mm)	height (mm)
5	10	5	5	0,5	5
5	4	2	5	0,5	5
5	2	1	5	0,5	5

4.3 Experimental results

In this section, the structure is studied as contact sensor, vibration sensor and proximity sensor. In addition, optical signal variation with temperature is characterized.

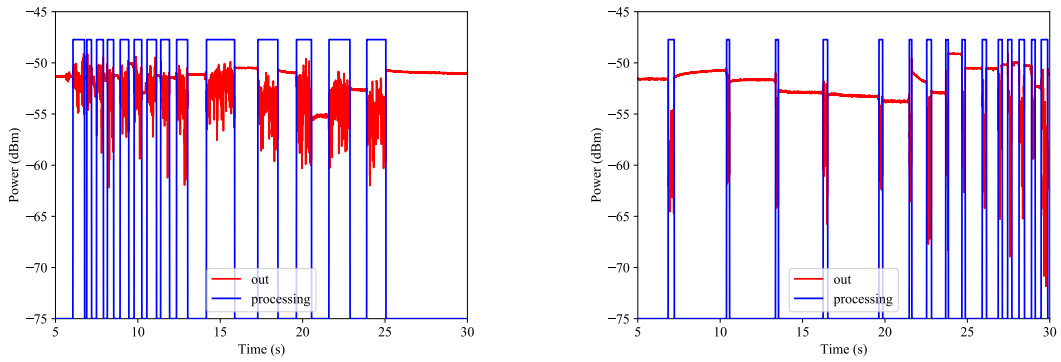
4.3.1 Contact Sensor

Based on the assembly scheme of figure 4.3, several tests have been made and in figure 4.4 is the best result obtained for each path.

In figure 4.4.A, the first elevation detection contains two grid elevations and thus was considered one third of the measured value for each elevation. The measurements are in table 4.2.

TABLE 4.2: Data obtained from figure 4.4.

Figure	Real dimension (mm)	Measurement	
		Average (mm)	Standard deviation (mm)
A	1	1.2	0.3
	2	2.2	0.2
	5	5	1
B	0.5	0.6	0.2



(A) (B)

FIGURE 4.4: Sensor response to contact with a grid: (A) path 1 and (B) path 2.

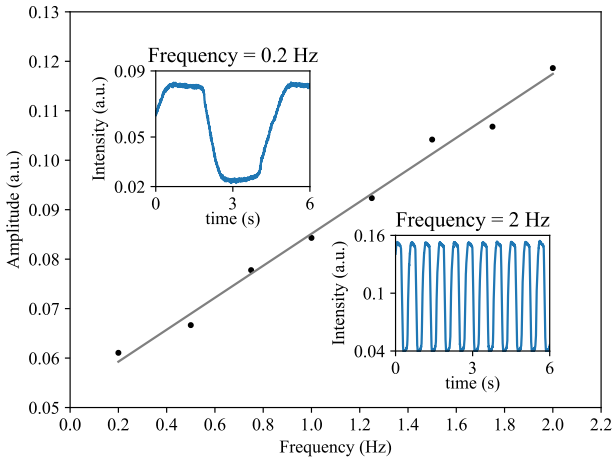


FIGURE 4.5: Sensor response to contact with an oscillating surface.

The analysis process consists of checking the place where the output signal variations are greater than the noise. If the average value remains unchanged, then the measurement is based on the variation of the air cavity between the tip and the sample (reflection) and if the average value changes (and some time returns to the initial average value) then the measurement consists of the tip contact with the sample. The standard deviation values associated the average value for the 2 mm is 9.1% and for the remaining perturbations is between 20% and 33%. These values result from the speed being little stable throughout the entire way and the fact that the geometry was held by the rod. The average obtained for each period, considering the standard deviations, coincides with the real dimensions which validates the results. Thus this geometry reveals the ability to determine the profile of the surface under study, namely for dimensions of the order of 2 mm.

4.3.2 Vibration sensor

In this characterization, the structure is permanently in contact with a black surface through the tip and this surface is coupled to an oscillator. For this, the setup of figure 4.3.A is used where the sample's holder is replaced by a dark plate which is coupled to a vibration generator. This surface is in sinusoidal oscillation, whose amplitude is less than 0.5 mm, and constant temperature. Measurements were made at the wavelength of 1570 nm. This results in the figure 4.5 where the linear fit has a slope of $0.032 \pm 0.001\ Hz^{-1}$ with a $r^2 = 0.991$. Therefore, besides being a contact sensor, is also a vibration sensor, where sensitivity increases with increasing frequency.

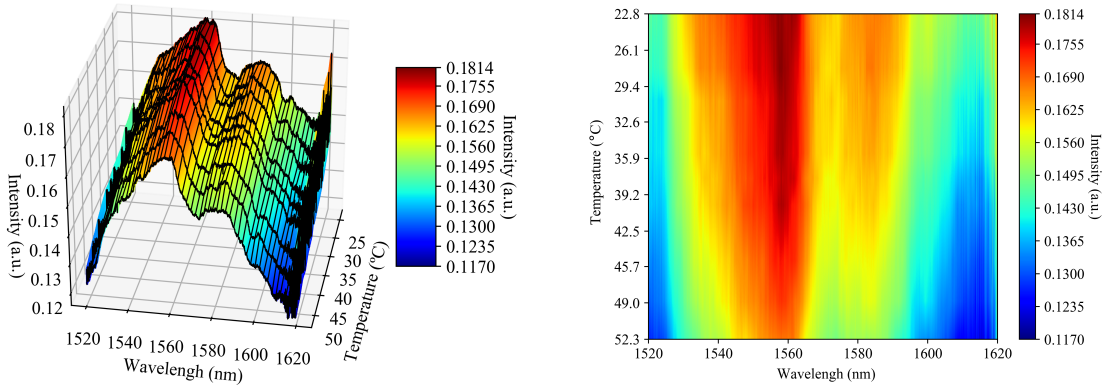


FIGURE 4.6: Sensor response to temperature variation: (A) in 3D and (B) in 2D.

The optical signal is a saturated sinusoid. Since the sensor was fixed by the rod at 25 mm to the geometry, so saturation occurs when the tip is subjected to the maximum curvature and the rod begin to bend. Thus, the tip keeps the curvature constant and consequently the optical signal remains constant.

4.3.3 Temperature characterization

The setup os figure 4.2 was used for temperature characterization. The results are in the figure 4.6.

The slope and r^2 of the linear fit were calculated to determine the sensitivity for each wavelength and for the entire temperature range under study whose values are shown

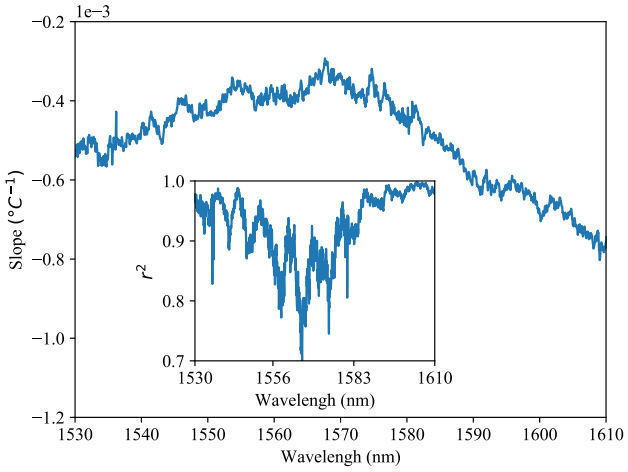


FIGURE 4.7: Features of linear adjustment of the normalization as a function of temperature for each wavelength under study.

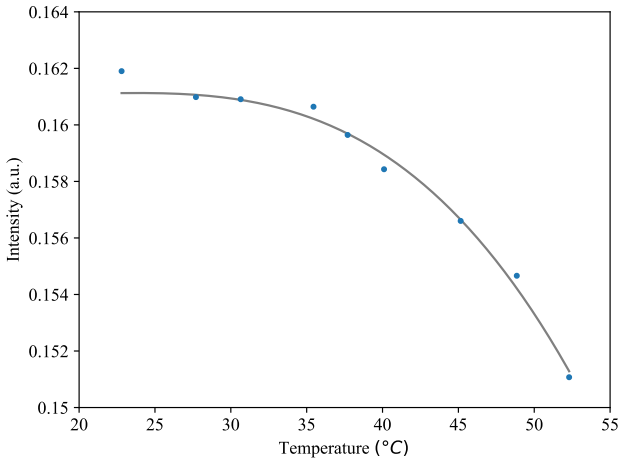


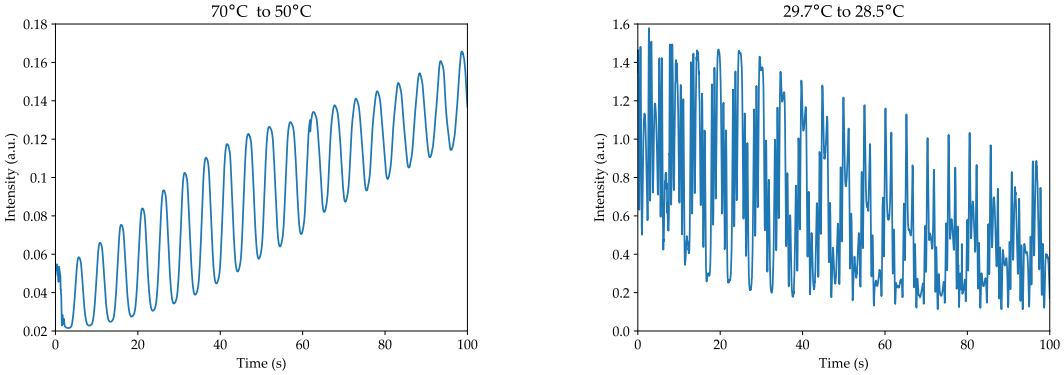
FIGURE 4.8: Sensor response for wavelength of 1570 nm as a function of temperature and cubic fit: $a_0 = 0.16 \pm 0.02$, $a_1 = (-0.000 \pm 0.002)\,^{o}C^{-1}$, $a_2 = (2 \pm 5)\,10^{-5}\,^{o}C^{-2}$, $a_3 = (-3 \pm 4)\,10^{-7}\,^{o}C^{-3}$ and $r^2 = 0.992$.

in the figure 4.7. As it can be seen, the sensitivity is minimum for wavelengths in the 1570 nm region and in the 1610 nm region the sensitivity is maximum.

In figure 4.8, the response at 1570 nm is nonlinear and the fit coefficients are mentioned in the graphic legend where $r^2 = 0.992$. The maximum variation of signal intensity for the temperature range under study is 0.009 which corresponds to 5.6 % of signal intensity at room temperature. Then, the sensor is insensitive to temperature.

Structure response when the tip is in contact with a hot surface

Considering that the previous study was related to the heating of the all structure, follows the study related to heating only the tip of the structure. For this, it was used the scheme of figure 4.3 but the grid was replaced by an aluminum hotplate. Given that it is impossible to eliminate all oscillations of the objects involved in the measurements, especially the low frequency, the heating plate was put in vibration with a amplitude of less than 0.5 mm and a frequency of 0.2 Hz. The plate was first heated and then tip stay permanent in contact with the plate. As we can see in figure 4.9.A, as the plate cools, the average signal intensity increases and the oscillation amplitude initially increases and then decreases leading to two hypotheses: (1) the tip is sensitive to thermal variation; (2) The measurements allow to evaluate the variation of the metal plate thickness during cooling. In the figure 4.9.B, the new optical signal contains several frequencies.



(A) (B)

FIGURE 4.9: Structure response when only the tip temperature is changed and is exposed to an oscillation of 0.2 Hz: cooling from 70 ^{o}C to 50 ^{o}C (A) and from 29.7 ^{o}C to 28.5 ^{o}C (B).

Thus, in figure 4.10 which is FFT of figure 4.9.B, there are several highs. Except for the continuous component, the absolute maximum occurs at the frequency of 0.2 Hz and the relative maximum with the second highest intensity occurs at 0.6 Hz.

This latter frequency occurs due to the constructive and destructive interference that exists in the approach and the distance of the sensor from the surface and which is shown in figure 4.11. Thus, the frequency of 0.6 Hz corresponds to the carrier wave and the frequency of 0.2 Hz corresponds to the signal resulting from surface vibration and modulate the carrier.

Since the optical signal shows the frequency associated with the surface (0.2 Hz) then this sensor can also operate in reflection mode, allowing to safeguard the integrity of the structure. For oscillation amplitudes below 10 μm, the signal will not show the frequency

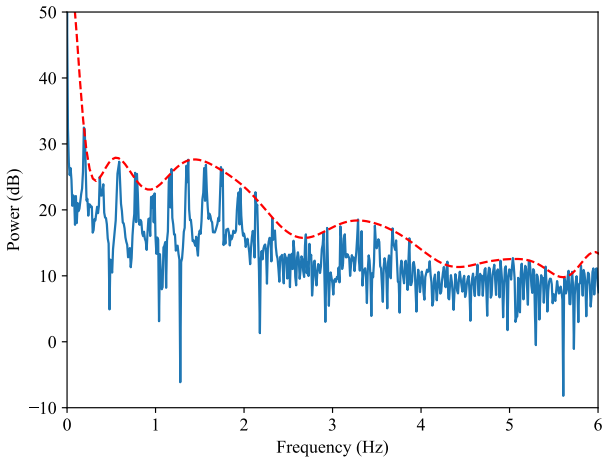


FIGURE 4.10: FFT from figure 4.9.B.

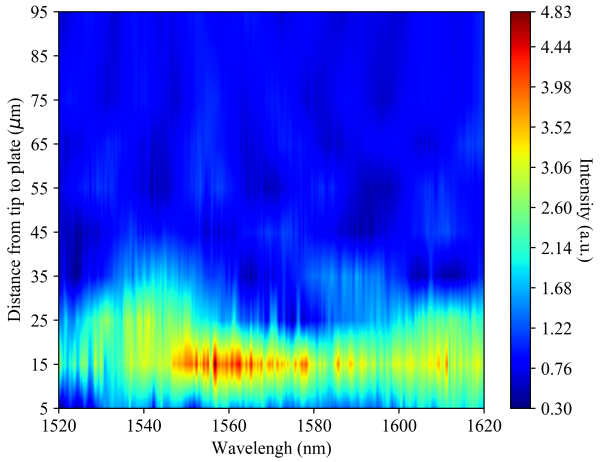


FIGURE 4.11: Structure response when approaching the aluminum plate.

associated with the interference condition and therefore do not existe carrier. In addition, the maximum reflection intensity occurs at $15\,\mu m$ which implies the tip works as a lens with a focal length of $15\,\mu m$ and given that the diameter is $13\,\mu m$ then the $NA = 0.43$.

4.4 Conclusion

So, this geometry allows the elaboration of contact sensors as an alternative solution to the current cantilever because allows the characterization of the surface profile with precision. The ability to determine the vibrations of a given surface has been demonstrated and for the frequency between $0.2\,Hz$ and $2\,Hz$, the linear sensitivity is $0.032 \pm 0.001\,Hz^{-1}$. Furthermore, it has been proved that temperature sensitivity is nonlinear and, for the study temperature range, is low. This geometry allows two operation modes, in reflection, which should be the first method to be used for determining the location of the surface perturbations and then the contact method for accurately gauging the three dimensions of the perturbation in question. Finally the ability to measure the thickness fluctuations of a given object due to temperature variation was verified and the geometry works as a lens with a focal length of $15\,\mu m$ and a $NA = 0.43$.

To improve the sensor performance, should be used thiner tips, which increases mechanical sensitivity, and coatings, which increases the output spectrum power and the number of possible optical paths. The good performance of this structure is due to the fact that the two optical paths are strongly influenced by the curvature of the tip, this is, the tip has a dimension that allows to be multimode. When the thickness is very reduced,

the tip may have a single optical path (or two optical paths whose path difference is too small to be observed in the spectral region under study). Thus, although there is an increase in mechanical sensitivity, this will have a smaller variation of the optical signal. One possible solution is that the structure be composed of a series multimode tip with a single mode tip much shorter than the multimode tip.

The sensor will have the greatest impact on replacing the cantilever currently used in AFM. However, the tip needs a optimization (size reduction). In addition, will allow the study of micro-processes in real-time and the determination of mechanical waves that propagate through buildings, bridges and tunnels, including seismic wave detection and characterization.

Chapter 5

New complex microstructures at the fiber optic end

5.1 Refractive index and low temperature sensors

5.1.1 Introdution

Today, refractive index determination is essential in controlling many applications in physics and chemistry. The refractive index provides an indirect mean of the liquid temperature [35, 36], determination of the number of particles as well as their dimensions [37], in the control of a chemical reaction [38, 39] even as in biosensor [40]. However, traditional refractometers, both in terms of their dimensions and the way they operate, which consists of determining the critical angle, present difficulties in micro-scale measurements as well as in non-transparent liquids. Thus, there has been an effort to develop a refractometer that not only achieves the micrometer scale but also allows real time analysis. One of the possibilities under study is the use of optical fibers for this task. To this end, systems have been used as metal coated fibers for the study of surface resonance plasmonics [41], Fiber Bragg Grating (FBG) [42] and taper [43], where all these systems are based on the decrease in light confinement leading to interaction with the external environment.

This chapter intends for the characterization of several structures produced in standard optical fiber for temperature and refractive index in liquids. Contrary to what was previously mentioned, the functioning of the following structures is based on the interaction of light with the external environment by means of the reflections of the diversions optical paths, which interfere between themselves. Thus, despite the insensitivity of the

spherical structure, the structures under analysis present an appreciable sensitivity, being the light intensity variation the most studied.

5.1.2 Setup configuration

In this work was used the splice machine "Sumitomo Electric Type-72C", the interrogation system used was an optical spectrum analyzer (OSA) "Advantest Q8384" with a resolution of 0.02 nm and a spectrum source in the 1550 nm region with a bandwidth of 50 nm.

Two types of measurements have been made: variation in external refractive index and temperature: from room temperature up to 100 ^oC.

Aqueous sugar solutions were used for refractive index characterization (figure 5.1). For each refractive index value a unique solution consisting of 100 ml distilled water and a portion of sugar was used. The data in the graph of the figure 5.2 refer to the characteristics of each solution immediately after manufacture. Thus, for each use of each solution the refractive index value was updated since the time distance between measurements using the same solution implied the existence of evaporation, so the concentration increased and consequently the refractive index also increased. For the refractive index characterization of the sensor, before immersing in the solution, the sensor was previously immersed in acetone and then in distilled water in order to remove possible crystallizations.

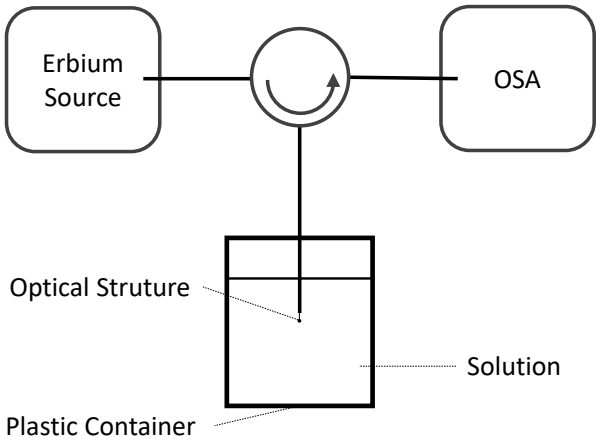


FIGURE 5.1: Setup scheme for characterisation of liquid refractive index variation.

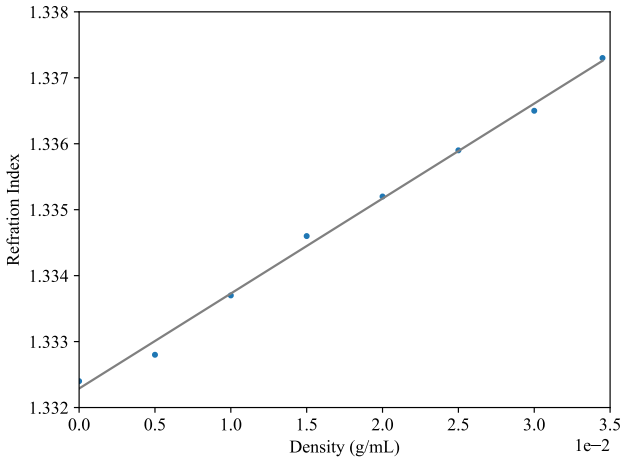


FIGURE 5.2: Calibration curve of the refractive index according to the density of dissolved sugar with a slope of $(0,137 \pm 0,004)\ R.I.U. \times \frac{ml}{g}$ and $r^2 = 0,995$.

For the temperature characterization the setup of figure 5.3 was used. Consists to insert the sensor into a capillary (to avoid possible damage to the structure) and placing inside a heating plate.

In this chapter, the sensors' characterization is mainly in intensity variation since the wavelength change of the spectrum is mostly nonlinear.

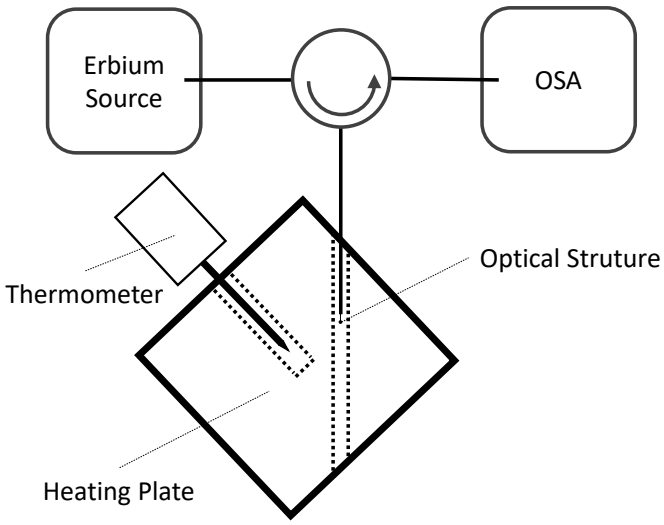


FIGURE 5.3: Setup schematic for temperature characterisation.

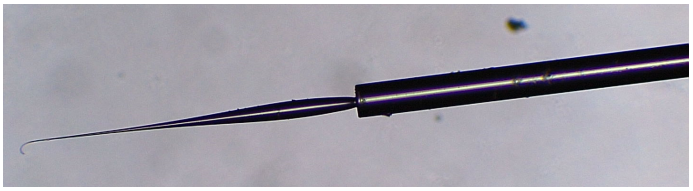


FIGURE 5.4: Narrow tip sensor geometry.

5.1.3 Narrow tip sensor

This sensor (figure 5.4) is composed of a tip with a length of 1.3 mm where the width of the connection to the rod is 38 μm, the widest part a width of 71 μm and the final part 2 μm.

This geometry was obtained according to the following steps:

- formation of two tips based on a taper (fuse two fibers with a power of $-80\,u.a.$ and stretch them until they separate, the duration of the process was 7 s); figure 5.5.(A) and (B);
- final tip fabrication (fusing one of the previous tips to a cleaved fiber; the arc application is on the fiber with the tip narrowed and distanced from the union about 250 μm so that the connection is not the widest part of this sensor; the thinner part results from the fiber stress being high and the electric arc having been disconnected at the same moment that the separation occurred); figure 5.5.(C) and (D).

The operation of this sensor consists of the beam dispersion that is caused by the narrow connection of the sensor to the cleaved fiber. Thus creates several optical paths that, due to length and surface curvature, implies that most of the reflection angles are large and consequently a greater number of reflections, enhancing the changes in the characteristics of the beam as a function of external characteristics. Given that the dimensions of

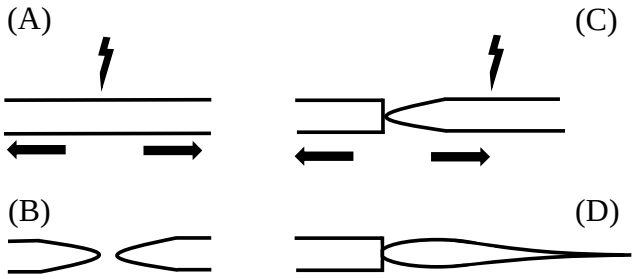
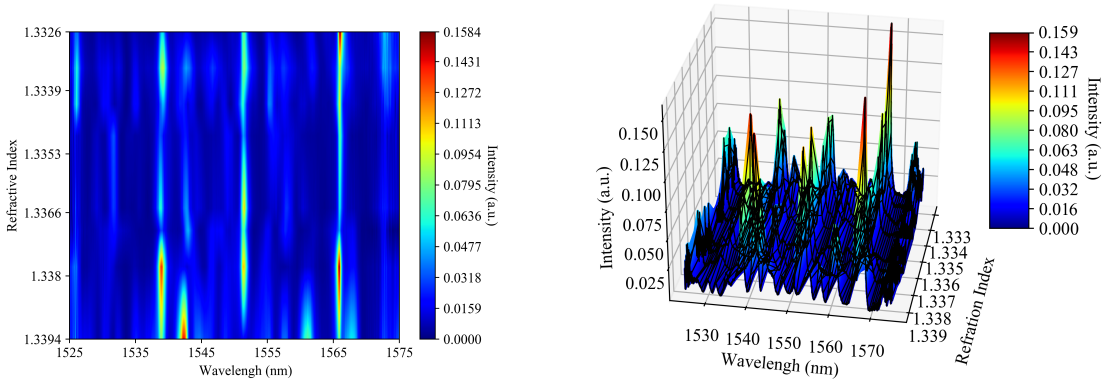


FIGURE 5.5: Manufacturing scheme of the narrow tip sensor.



(A) (B)

FIGURE 5.6: Output beam intensity as a function of the liquid refractive index for each wavelength: (a) in 3D and (b) in 2D.

the structure implies that the beam is strongly confined and therefore the effective refractive index is close to the silica refractive index, so the interaction is mostly a consequence of the several reflections of optical paths.

5.1.3.1 Experimental results

The characterization of this sensor as to the variation of the liquid refractive index for the range of [1.3326 , 1.3393] resulting in the graphics of figure 5.6.

After calculating the value of r^2, for all wavelengths in the entire refractive index range, is concluded that the relationships are cubic and that the wavelength with best cubic adjustment is 1541.78 nm (figure 5.7), whose data of the adjustment is found in the figure's legend. The maximum sensitivity obtained at this wavelength is 66.6 $R.I.U.^{-1}$.

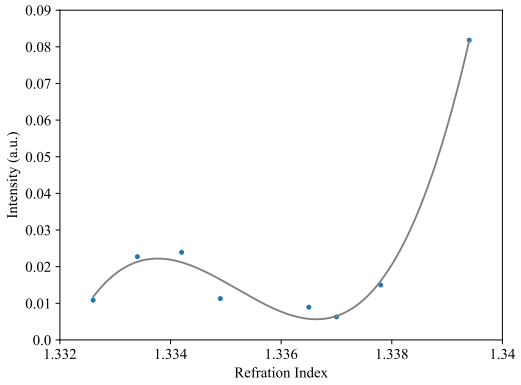
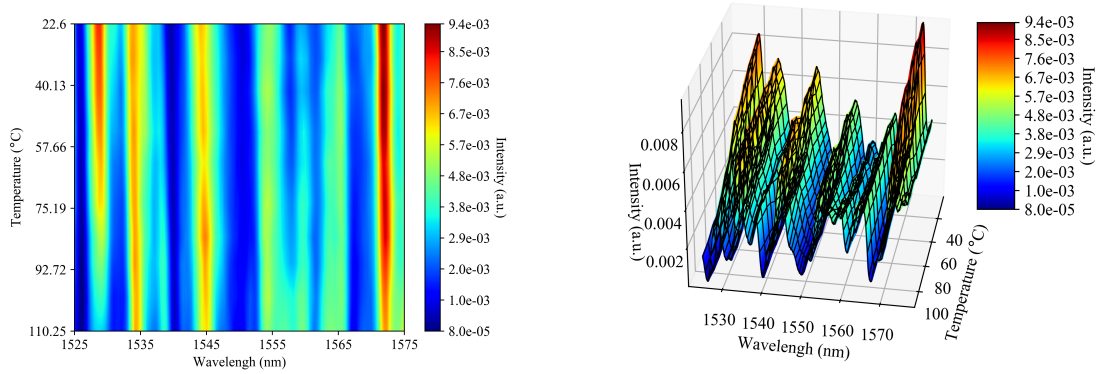


FIGURE 5.7: Narrow tip sensor response for wavelength of 1541.78 nm and cubic fit: $a_3 = (1.4 \pm 0.1)\, 10^6\, R.I.U.^{-3}$, $a_2 = (-5.6 \pm 0.6)\, 10^6\, R.I.U.^{-2}$, $a_1 = (7.5 \pm 0.8)\, 10^6\, R.I.U.^{-1}$, $a_0 = (-3.3 \pm 0.3)\, 10^6$ and $r^2 = 0.990$.



(A) (B)

FIGURE 5.8: Output beam intensity as a function of temperature for each wavelength: (A) in 3D and (B) in 2D.

In the characterization with the external temperature variation within the range of $[22.6\,,\,110.25]\ (^{o}C)$ result the graphs of figure 5.8.

There are linear relations and they are mainly located in wavelengths close to $1530\,nm$ where the wavelength with better linear adjustment is $1532.84\,nm$ (figure 5.9) whose data referring to the adjustments are in the figure legend. The sensitivity obtained for this wavelength is $3.51\ \left(10^{-5}\,^{o}C^{-1}\right)$.

In addition, the relative extreme located at $1544.10\,nm$ (figure 5.10) have a linear shift to higher wavelengths with a sensitivity of $8.8\ \left(pm\,^{o}C^{-1}\right)$. In this case the slope is positive, therefore the dominant term is thermal expansion.

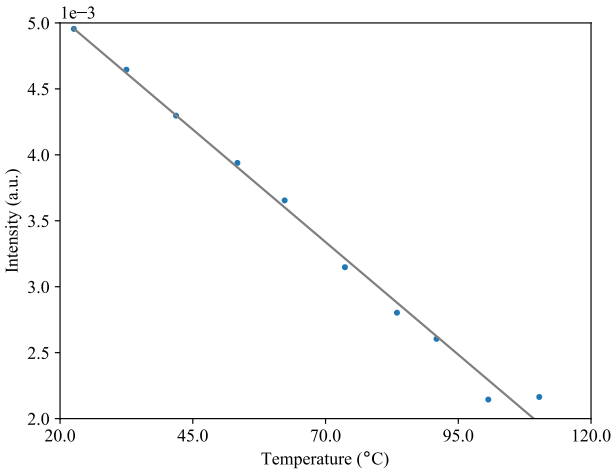


FIGURE 5.9: Narrow tip sensor response for wavelength of $1532.84\,nm$ and linear fit: $a_1 = (-3.51 \pm 0.06)\ 10^{-5}\,^{o}C^{-1}$, $a_0 = (5.60 \pm 0.04)\ 10^{-3}$ and $r^2 = 0.998$.

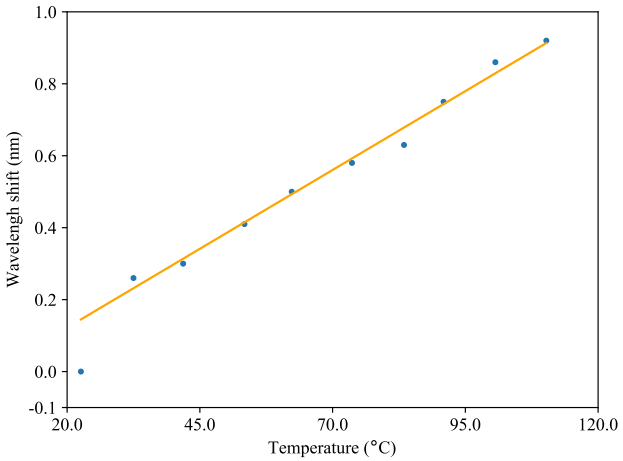


FIGURE 5.10: Relative extreme shift which, for the output spectrum related to room temperature, is 1544.10 nm and linear fit: $a_1 = (8.8 \pm 0.3)\,10^{-3}\,nm^{o}C^{-1}$, $a_0 = (-5 \pm 3)\,10^{-2}\,nm$ and $r^2 = 0.990$.

5.1.4 Wide tip sensor

This sensor (figure 5.11) approximates the characteristics of the previous sensor. Consists of a tip with a length of 865 μm where the width of the connection to the rod is 20 μm, the wider part 52 μm and the thinner part 17 μm.

The manufacturing method involves the following steps:

- fabrication of two tips based on a taper: fusion of two fibers with a power of $-80\,u.a.$ and stretch them until they separate, forming two tips; the duration of the process depends on the tension applied to the fiber; in this work was 7 s (figure 5.12.(A) and (B));

- formation of the final tip: fuse one of the previous tips to a cleaved fiber; the application of the arc is in the fiber with the narrowed tip and is about 300 μm away from the connection; the final part is rounded because the arc has been turned off 0.5 s after the instant when the division occurs (figure 5.12.(C) and (D)).

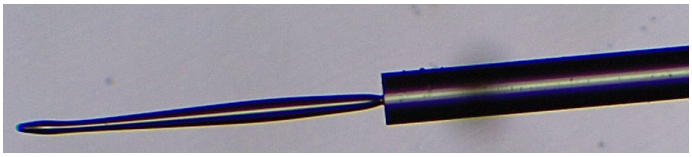


FIGURE 5.11: Wide tip sensor geometry.

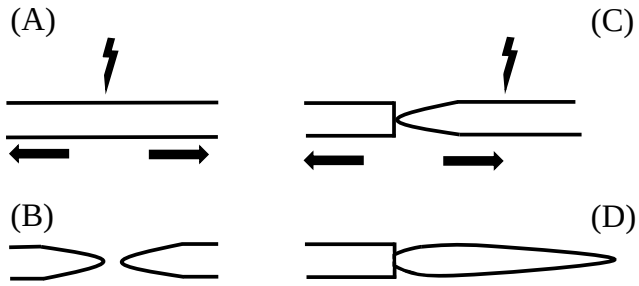
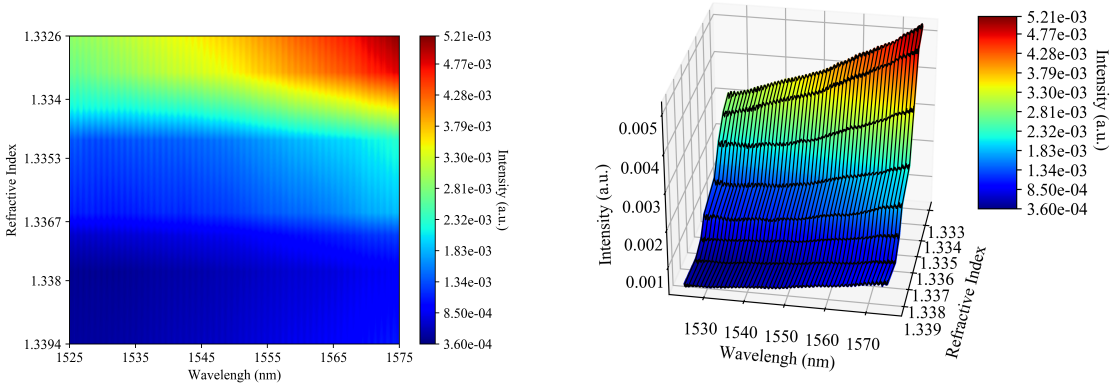


FIGURE 5.12: Manufacturing scheme of the wide tip sensor.

Similar to the previous sensor, the beam is scattered due to the close connection causing excitation of some modes. Based on the experimental results below, the fringes with the highest intensity have a distance between maximums greater than 50 nm which implies that the difference between the two most intense optical paths is less than 15 μm. That is, considering the dimensions of the sensor, the difference in optical paths results from the geometry of the end of the sensor that is close to the ellipsoid that is not aligned with the fiber core.

5.1.4.1 Experimental results

The results of characterization in the liquid refractive index for the range [1.3326 , 1.3394] are in figure 5.13. The spectrum contains several fringes, some with a bandwidth higher than 50 nm and others with a bandwidth of 1 nm.



(A) (B)

FIGURE 5.13: Wide tip sensor response as a function of the liquid refractive index for each wavelength: (A) in 3D and (B) in 2D.

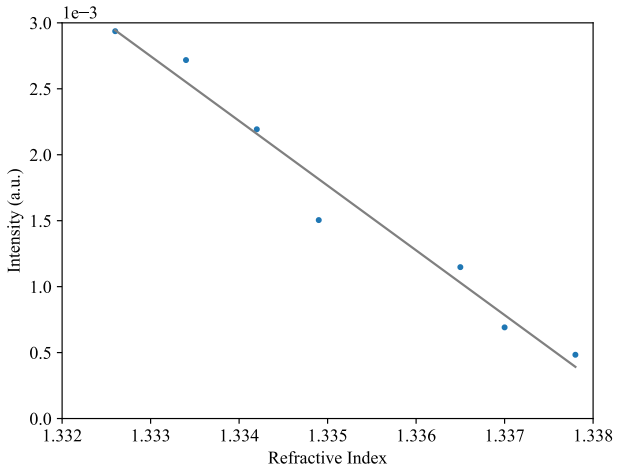


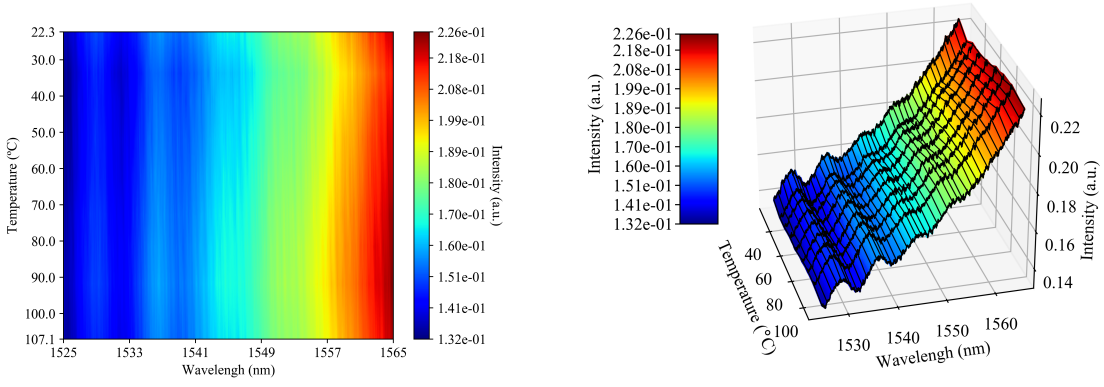
FIGURE 5.14: Wide tip sensor response for wavelength of 1525.00 nm and linear fit: $a_1 = (0.49 \pm 0.04)\ R.I.U.^{-1}$, $a_0 = 0.66 \pm 0.05$ and $r^2 = 0.97$.

The wavelengths with good linear adjustment are close to 1525 nm and the wavelength with a good r^2 is 1525.00 nm (figure 5.14) whose data of the adjustment is found in the figure's legend. For this wavelength, the sensitivity is 0.49 $R.I.U.^{-1}$.

Characterizing the sensor in a low temperature range ($[22.3\,,\ 107.0]\ (^oC)$) the graphs from figure 5.15 were obtained:

In this case the relations are mostly cubic in the whole wavelength range under study where the best adjusted wavelength is 1564.09 nm (figure 5.16), whose data of the adjustments are in the legend of the figure. The maximum sensitivity is 4.47 $\left(10^{-4}\ ^oC^{-1}\right)$.

In figure 5.16 can be seen that there is an intensity modulation of the interferometer fringe with a frequency of 0.01 $^oC^{-1}$.



(A) (B)

FIGURE 5.15: Wide tip sensor response as a function of temperature for each wavelength: (A) in 3D and (B) in 2D.

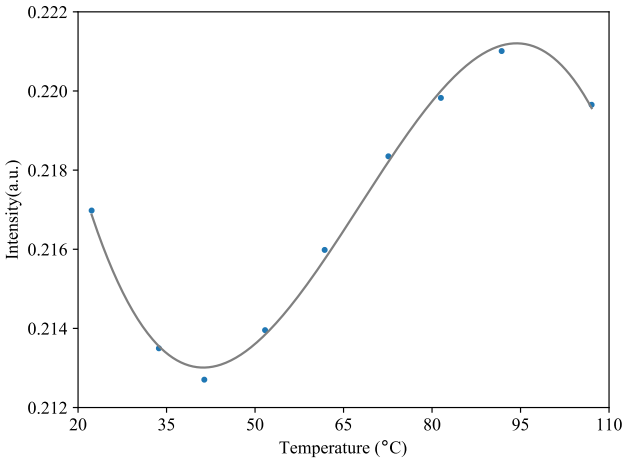


FIGURE 5.16: Wide tip sensor response for wavelength of 1564.09 nm and cubic fit: $a_3 = (-1.09 \pm 0.05)\,10^{-7}\,R.I.U.^{-3}$, $a_2 = (2.2 \pm 0.1)\,10^{-5}\,R.I.U.^{-2}$, $a_1 = (-1.28 \pm 0,06)\,10^{-3}\,R.I.U.^{-1}$, $a_0 = 0.235 \pm 0.001$ and $r^2 = 0.997$.

The relative extremes of this sensor, in both characterizations, have non-linear behaviors.

5.1.5 Dual-microsphere and tip sensor

The sensor of figure 5.17 consists of two microspheres, one with a diameter of 181 μm and the other with a diameter of 73 μm and a tip with a length of 57 μm where the final part has a width of 3.5μm. The connection between the microspheres has a width of 54 μm and the connection between the microsphere and the tip has a width of 13 μm.

The manufacturing method consists of the following steps:

- formation of the wide microsphere: apply an electric arc with a power of 50 $u.a.$ and a duration of 10 s to form the highest microsphere;

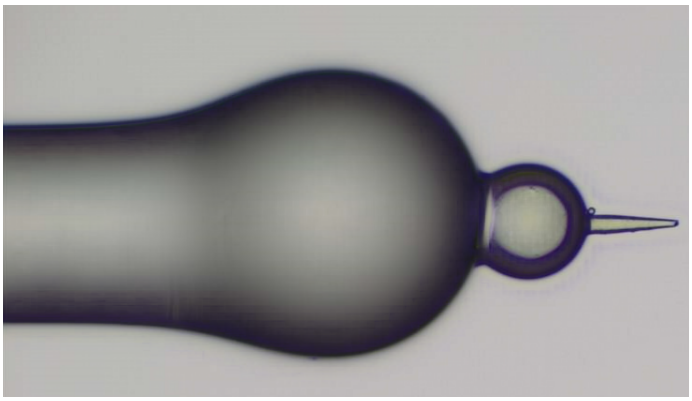


FIGURE 5.17: Dual-microsphere and tip sensor geometry.

- fabrication of two tips based on a taper: fuse two fibers with a power of $-40\,u.a.$ and stretch them until they separate, giving rise two tips; this work had a duration of $8\,s$;
- fuse this tip to the microsphere by applying an electric arc to the tip rod. The formation of the second microsphere occurs if the application of the electric arc is maintained after the formation of the tip in the larger microsphere (figure 5.18.A and B);
- formation of the final tip: fuse one of the previous tips to the smaller diameter microsphere; the application of the arc is on the rod of the tip and should be switched off when the fibers are separated (figure 5.18.C and D).

The sensor's operation consists in the dispersion of the beam that is caused by the first microsphere. Then there are two types of paths: one due to reflection and the other due to beam transmission to the second microsphere and, consequently, to the tip. Unlike the previous structures where the main characteristic is the long length, this is the fact that the sensor consists on three structures in series.

5.1.5.1 Experimental results

The results of characterization in the liquid refractive index for the range $[1.3327\,,\,1.3396]$ are in the figure 5.19.

For the refractive index of 1.3367, a mode loss occurs which leads to a change in the output spectrum profile.

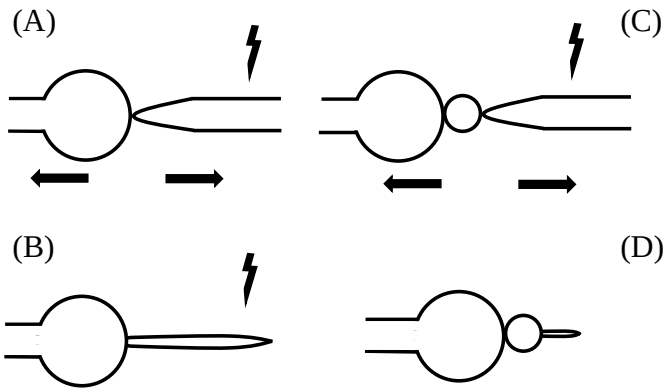
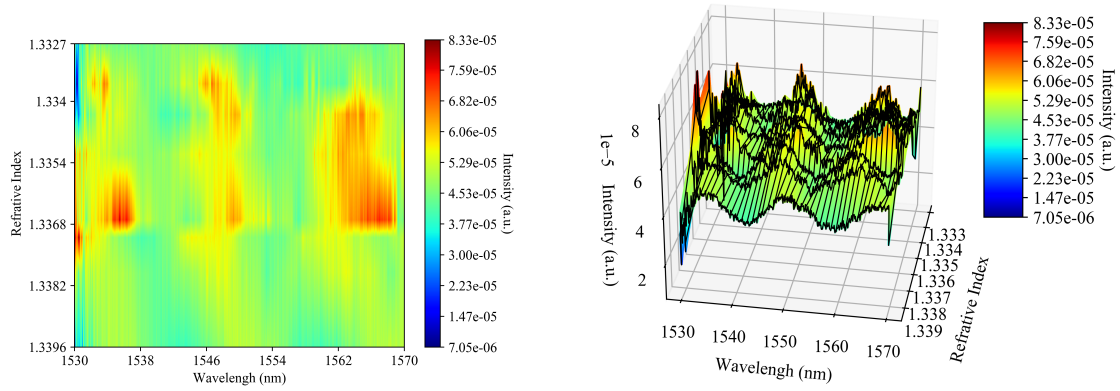


FIGURE 5.18: Manufacturing scheme of the dual-microsphere and tip sensor.



(A) (B)

FIGURE 5.19: Dual-microsphere and tip sensor response as a function of the liquid refractive index for each wavelength: (a) in 3D and (b) in 2D.

The wavelengths with a good cubic adjustment belong to the range $[1545\,,\,1560]\,(nm)$ and the wavelength with a good cubic adjustment is $1554.59\,nm$ (figure 5.20) which the adjustment data are in the figure legend. The maximum sensitivity for this wavelength is $1.16 \times 10^{-2}\,R.I.U.^{-1}$.

The results of this sensor characterization in a low temperature range, $[22.4\,,\,123.4]\,(^{o}C)$, are in the figure 5.21.

The wavelengths with linear adjustment are: $[1525\,,\,1530]\,(nm)$, $[1535\,,\,1545]\,(nm)$, $[1550\,,\,1560]\,(nm)$ and $[1565\,,\,1570]\,(nm)$. The wavelength with a good linear adjustment is $1554.45\,nm$ (figure 5.22), whose adjustment data is found in the figure legend. For this wavelength, the sensitivity is $(6.6 \pm 0.2)\,10^{-5}\,{}^{o}C^{-1}$.

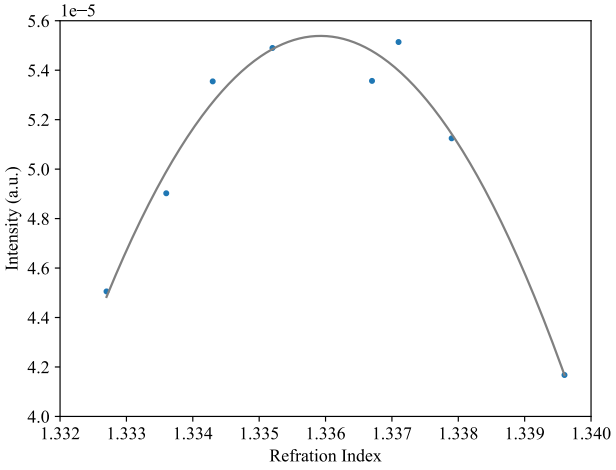
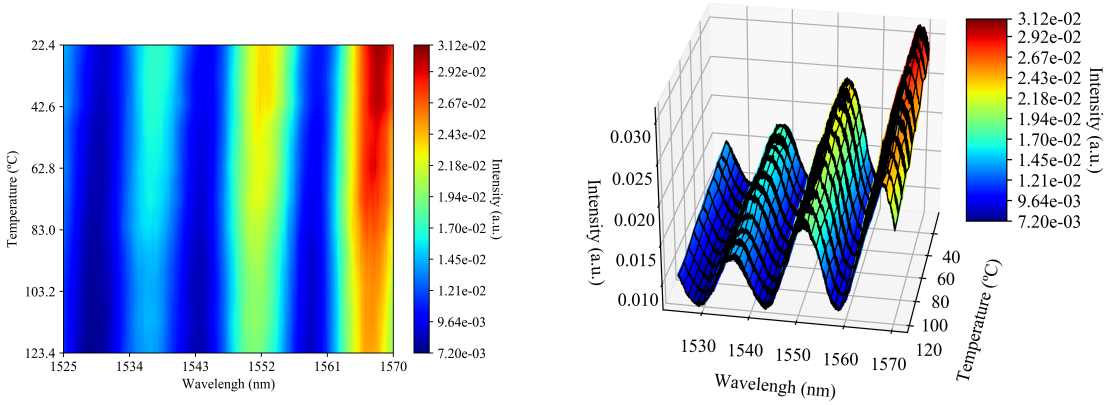


FIGURE 5.20: Dual-microsphere and tip sensor response for wavelength of $1554.59\,nm$ and cubic fit: $a_3 = (1.3 \pm 0.3)\,10^2\,R.I.U.^{-3}$, $a_2 = (-5 \pm 1)\,10^3\,R.I.U.^{-2}$, $a_1 = (7 \pm 1)\,10^3\,R.I.U.^{-1}$, $a_0 = (-3.2 \pm 0,6)\,10^3$ e $r^2 = 0.994$.



(A) (B)

FIGURE 5.21: Output beam intensity as a function of temperature for each wavelength: (A) in 3D and (B) in 2D.

In addition, the extreme located in the wavelength of 1530.37 nm suffers a shift (figure 5.23). This shift is linear with the rise in temperature and the sensitivity is 20.0 $\left(pm\,^{o}C^{-1}\right)$.

Since the slope is negative, then the dominant term is the thermo-optic coefficient.To finish this analysis, the maximum sensitivity obtained are synthesized in the table 5.1 as well as the correlation values of the adjustments presented for each sensor.

TABLE 5.1: Sensors features for intensity characterization: maximum sensitivity and r^2.

Sensor	Refractive Index		Temperature	
	sensitivity $\left(R.I.U.^{-1}\right)$	r^2	sensitivity $\left(^{o}C^{-1}\right)$	r^2
narrow tip	**66.6**	0.997	3.51×10^{-5}	0.998
wide tip	0.49	0.97	$\mathbf{4.47 \times 10^{-4}}$	0.997
dual-microsphere and tip	1.16×10^{-2}	0.994	6.6×10^{-5}	0.993

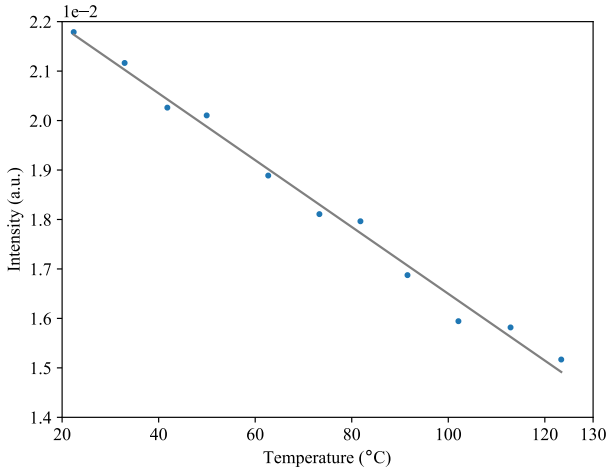


FIGURE 5.22: Dual-microsphere and tip sensor response for wavelength of 1554.45 nm and linear fit: $a_1 = -6.6 \pm 0.2\,\left(10^{-5}\,^{o}C^{-1}\right)$, $a_0 = 2.33 \pm 0.02\,\left(10^{-2}\right)$ e $r^2 = 0.990$.

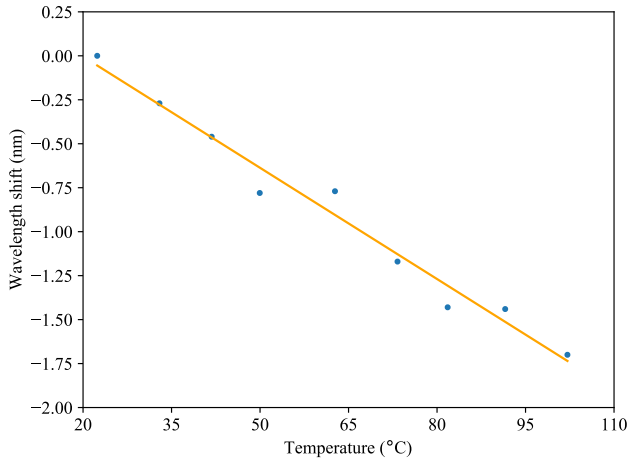


FIGURE 5.23: Relative extreme shift which, for the output spectrum referring to the lowest refractive index, is located at wavelength 1530.57 nm and linear fit: $a_1 = (-0.020 \pm 0.001)\, nm\, ^oC^{-1}$ e $a_0 = (0.42 \pm 0.09)\, nm$ and $r^2 = 0.97$.

The sensor with tip geometry is the one that has the highest sensitivity to the variation of the refractive index of a liquid. This is due to the fact that the length of this sensor is the longest of the three sensors and that the average width of this sensor is the shortest of the three, allowing for higher interaction between the beam and the outside. However, for temperature variation, the sensor with the highest sensitivity is the wide tip sensor. This is due to the fact that this sensor is larger than the previous structure and is also longer where the optical paths are mainly influenced by variations in sensor dimensions due to thermal expansion. The last sensor, although having lower sensitivity in both characterizations, revealed higher mechanical resistance.

5.1.6 Conclusion

From table 5.1, is concluded that the best sensor for measuring the refractive index is the narrow tip geometry sensor, the sensor with good performance for measuring the temperature between the room temperature and 100 ^oC is the wide tip sensor and the most robust sensor is the dual-microsphere and tip sensor. In addition, most of the spectrum extremes have non-linear behavior except for two extremes, one in the tip geometry sensor and the dual-microsphere and tip sensor, both for temperature variation. For the first sensor, in terms of extreme shift, the dominant term is thermal expansion, while for the third sensor the dominant term is the thermo-optic coefficient.

The high advantage of this type of sensors is the easy production and application, being that the measurement area is in the order of μm^2 allowing the fast and precise scan of a fast and precise mapping of a given structure in terms of temperature and liquid refractive index, being able to indirectly control other characteristics of the surrounding environment.

5.2 High temperature sensors

5.2.1 Introduction

Nowadays, thermal sensors are important in the operation of mechanical and electronic systems in order to control the efficiency of macroscopic and microscopic systems as well as in the control of their cooling. In addition, there has been much demand for environmental monitoring in order to understand the impact of global warming on the ecosystem [44]. Despite these needs, electronic thermal sensors, such as thermocouples, demonstrate measurement problems when exposed to electromagnetic fields, chemical and mechanical disturbances that exist in micrometric systems and the environment. For this reason it has been verified the power of optical measurements, more properly the optical fiber.

In this work, two fiber optic structures will be tested that have the ability to measure in real time, have mechanical robustness and the measurement area is in the order of μm^2, allowing a three-dimensional mapping of micro-systems in addition to being insensitive to external electromagnetic fields. The working principle of these sensors is an interferometer.

5.2.2 Setup configuration

The splice machine "Sumitomo Eletric Type-72C" was used to manufacture the sensors. For the characterization, it was used the optical spectrum analyzer (OSA) "Advantest Q8384" with a resolution of 0.02 nm and a wide spectrum source in the region of 1550 nm with a width of 50 nm.

For dual-microsphere, taper and tip sensor, the characterization was for temperatures between room temperature and 400 ^oC and for tip sensor from room temperature up to 600 ^oC. For these two characterizations, the diagram of figure 5.24 was used. Both sensors were placed in capillaries (to avoid possible damage to the structure) and this is placed inside an oven.

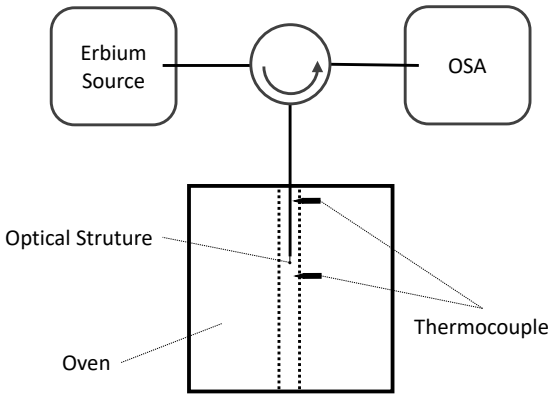


FIGURE 5.24: Setup schematic for temperature variation characterisation.

5.2.3 Dual-microsphere, taper and tip sensor

This sensor (fig 5.25) consists of two microspheres and two tips. One is responsible for connecting the larger microsphere to the cleaved fiber with a length of 128 μm where the wider part has a width of 54 μm and the final part 21 μm. The other at the end of the sensor that has a length of 61 μm, the connection has a width of 6 μm and the larger part 16 μm. The greater microsphere has a diameter of 138 μm and the smaller microsphere, which has been stretched to the following dimensions: length of 105 μm, width of the thinner part of 51 μm and the larger part of 70 μm.

Manufacturing follows these steps:

- formation of two tips (fuse two fibers with a power of $-80\,a.u.$ and stretch them until they separate forming two tips; the process duration depends on the tension applied to the fiber; in this work was of $7\,s$);



FIGURE 5.25: Dual-microsphere, taper and tip sensor geometry.

- fuse one of the tips to a cleaved fiber to form the link between the microsphere and the cleaved fiber (figure 5.26.A);
- Fuse another fiber cleaved to the previous point's fiber. The arc should be applied away from the union and on the new cleaved fiber. At the same time, apply a tension that will lead to the separation and consequent annexing of a fiber portion to the tip. The continuity of the electric arc application will take the spherical form and therefore the formation of the larger microsphere(figure 5.26.B);
- Repeat the previous point with the following changes: cleaved fiber becomes the narrowed fiber left over from the first point and this is fused to the microsphere. The geometry is close to an ellipsoid since the arc duration was 5 s (figure 5.26.C);
- Then a new type was created based on the first step;
- fabrication of the final tip: the application of the arc is on the tip's rod and it must be turned off when the fibers are separated (figure 5.26.D e 5.26.E).

The taper that connects the fiber to the first microsphere has two functions: to decrease the confinement of the beam in the fiber core by increasing the interactions with the outside and to decrease the cone of reflected light admission allowing to remove optical paths that would lead to the degradation of the signal due to the low power. The first microsphere is responsible for dispersing the beam leading to the excitation of several modes in the second microsphere.

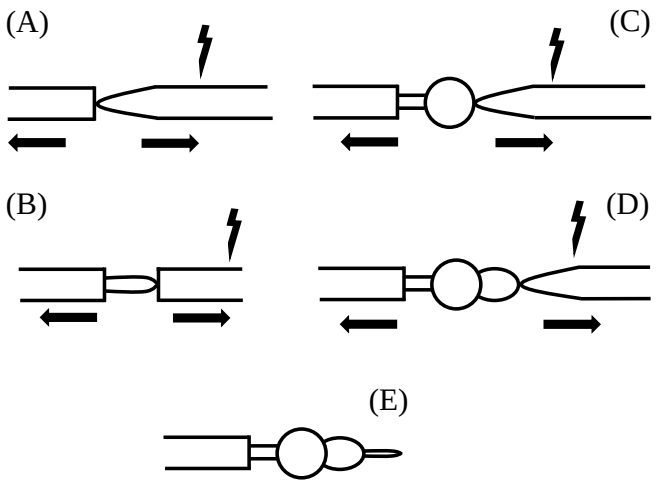
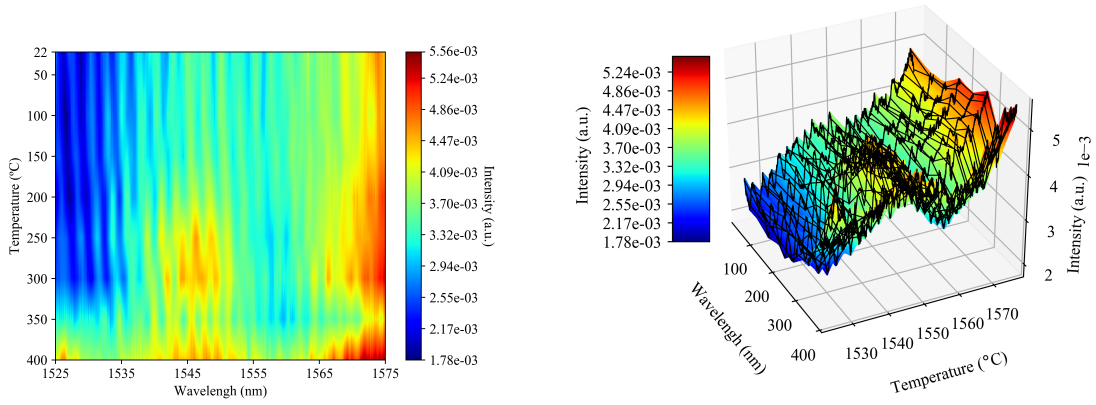


FIGURE 5.26: Manufacturing scheme of the dual-microsphere, taper and tip sensor.



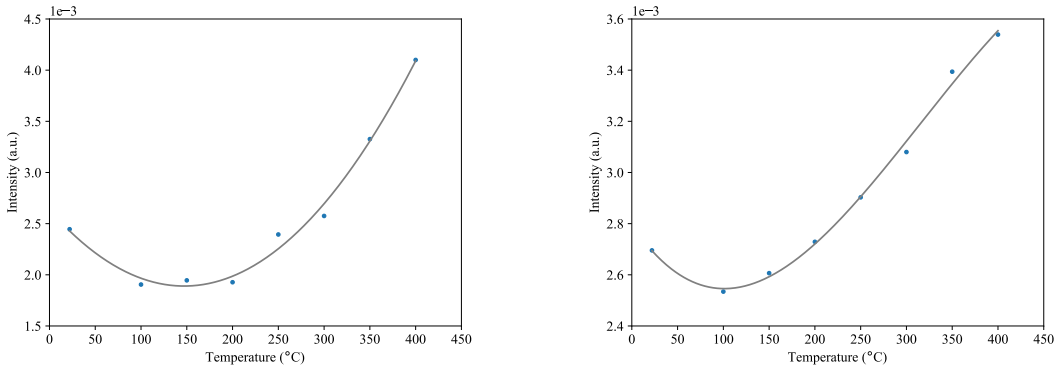
(A) (B)

FIGURE 5.27: Dual-microsphere, taper and tip sensor response as a function of temperature for each wavelength: (A) in 3D and (B) in 2D.

5.2.3.1 Experimental results

In characterization of this sensor in a temperature range $[22\,,\,400]\,(^oC)$, the figure 5.27 were obtained.

In this characterization, for the variation in intensity, the relations are quadratic and cubic, where, for both, the wavelengths with better r^2 are: $[1525\,,\,1555]\,(nm)$. The wavelength with the best square adjustment is $1526.90\,nm$ with a maximum sensitivity of $1.74\,\left(10^{-5}\,^oC^{-1}\right)$ (figure 5.28.A) and the wavelength with best cubic adjustment is $1534.24\,nm$ with a maximum sensitivity of $4.52\,\left(10^{-6}\,^oC^{-1}\right)$ (figure 5.28.B).



(A) (B)

FIGURE 5.28: Dual-microsphere, taper and tip sensor response for wavelength: (a) $1526,90\,nm$ and square fit: $a_2 = (-3.4 \pm 0.2)\,10^{-8}\,^oC^{-2}$, $a_1 = (-1.0 \pm 0.1)\,10^{3}\,^oC^{-1}$, $a_0 = (2.6 \pm 0.1)\,10^{3}$ and $r^2 = 0.990$; (b) $1534.24\,nm$ and cubic fit: $a_3 = (-3.3 \pm 0.9)\,10^{-11}\,^oC^{-3}$, $a_2 = (3.1 \pm 0.6)\,10^{-8}\,^oC^{-2}$, $a_1 = -5 \pm 1\,\left(10^{-6}\,^oC^{-1}\right)$, $a_0 = (2.80 \pm 0.05)\,10^{-5}$ e $r^2 = 0.990$.

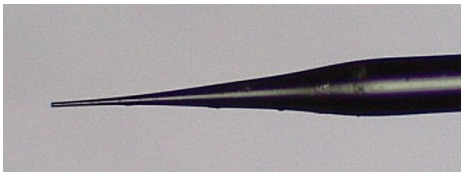


FIGURE 5.29: Tip sensor geometry.

5.2.4 Tip sensor

This sensor is a tip (figure 5.29), a length of 705 μm where the thinner part has a width of 9 μm.

The manufacturing process consists in the fabrication of two tips based on a taper: fusion of two fibers with a power of $-80\,u.a.$ and stretch them until they are separated forming two tips. This process had a duration of $7\,s$ (figure 5.30).

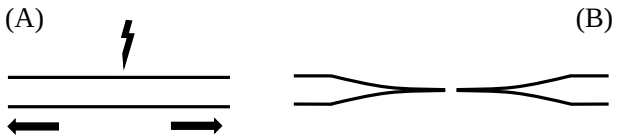
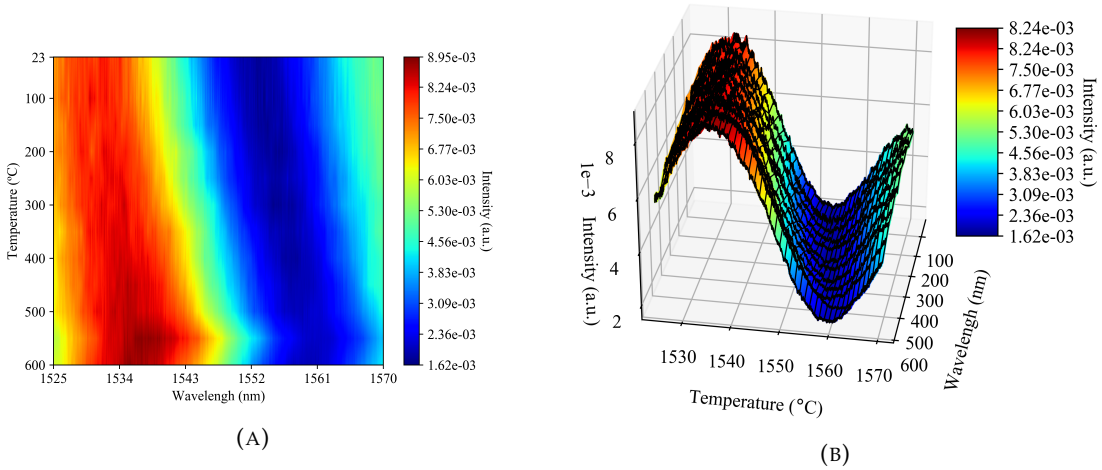


FIGURE 5.30: Manufacturing scheme of the tip sensor.

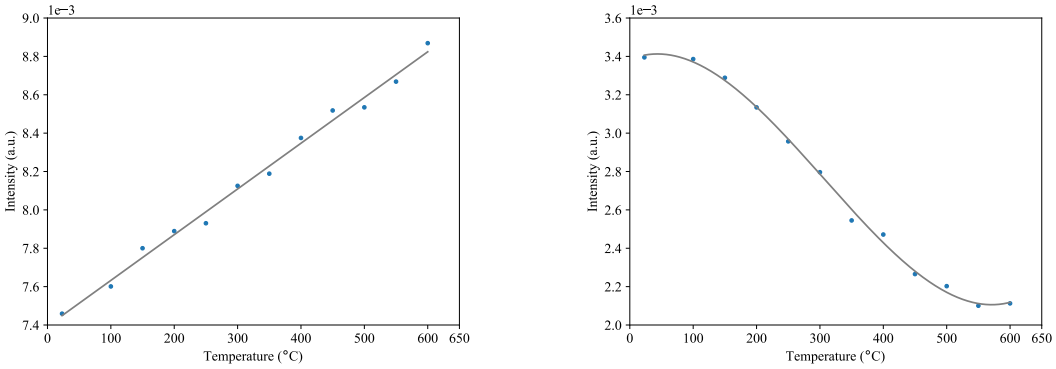
In the characterization of this sensor for the temperature range $[22\,,\,600]\,(^{o}C)$ were obtained the graphs of figure 5.31.

In this characterization, the relationships are mostly linear and cubic. The wavelengths with a good linear relation are in the $[1535\,,\,1555]\,(nm)$ and the wavelength with a good linear adjustment is 1535.34 nm with a sensitivity of 2.38 $\left(10^{-6}\,{}^{o}C^{-1}\right)$ (figure 5.32.a).



(A) (B)

FIGURE 5.31: Tip sensor response as a function of temperature for each wavelength: (A) in 3D and (B) in 2D.



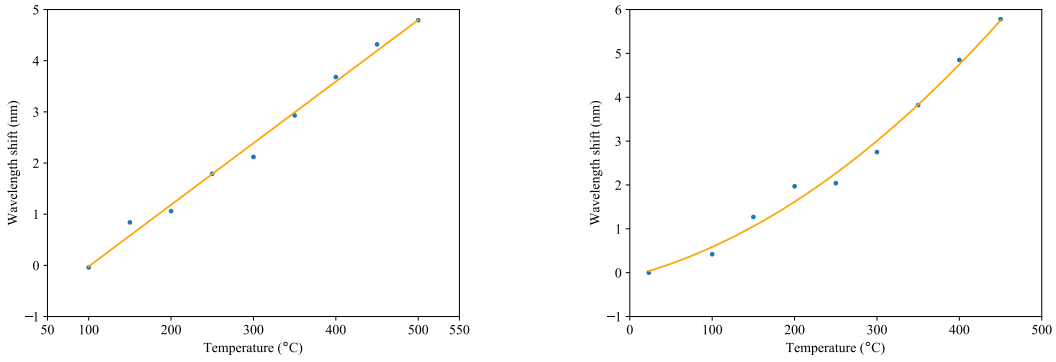
(A) (B)

FIGURE 5.32: Tip sensor response for wavelength: (A) 1535.34 nm and linear fit: $a_1 = (2.38 \pm 0.07)\,10^{-6}\,^{o}C^{-1}$, $a_0 = (7.39 \pm 0.03)\,10^{-3}$ and $r^2 = 0.991$; (B) 1561.88 nm and cubic fit: $a_3 = (1.8 \pm 0,2)\,10^{-11}\,^{o}C^{-3}$, $a_2 = (-1.6 \pm 0.2)\,10^{-8}\,^{o}C^{-2}$, $a_1 = (1.3 \pm 0.5)\,10^{-6}\,^{o}C^{-1}$, $a_0 = (3.38 \pm 0.04)\,10^{-5}$ and $r^2 = 0.997$.

The wavelengths with the best cubic relation are in the interval $[1560\,,\,1570]\,(nm)$, while the wavelength with the best cubic adjustment is 1561.88 nm with a sensitivity of 3.72 $\left(10^{-6}\,^{o}C^{-1}\right)$ (figure 5.32.b). In addition, the maximum at 1530.74 nm, at room temperature, has a sensitivity of 12 $\left(pm\,^{o}C^{-1}\right)$ and the minimum at 1553.02 nm has a maximum sensitivity of 22 $\left(pm\,^{o}C^{-1}\right)$ (figure 5.33).

In addition, the extremes move to longer wavelengths, then the dominant term is thermal expansion.

To finalize the intensity characterizations, table 5.2 synthesizes the maximum sensitivities obtained as well as the correlation values of the adjustments presented for each



(A) (B)

FIGURE 5.33: Relative extreme shift which, for the output spectrum related to the room temperature, is in the wavelength: (a) 1530.81 nm and linear fit: $a_1 = (1.20 \pm 0.04)\,10^{-2}\,nm^{o}C^{-1}$, $a_0 = (-1.2 \pm 0.1)\,nm$ and $r^2 = 0.992$; (b) 1553.02 nm and square fit: $a_2 = (1.7 \pm 0.2)\,10^{-5}\,nm^{o}C^{-1}$, $a_1 = (5 \pm 1)\,10^{-3}\,nm^{o}C^{-1}$, $a_0 = (-0.08 \pm 0.1)\,nm$ and $r^2 = 0.997$.

sensor.

TABLE 5.2: Características dos sensores quanto à caracterização em intensidade.

Sensor	Temperature	
	sensitivity $\left(^{o}C^{-1}\right)$	r^2
dual-microsphere, taper and tip	$\mathbf{1.74 \times 10^{-5}}$	0.995
Tip	3.72×10^{-6}	0.997

As can be seen, the dual-microsphere, taper and tip sensor is more sensitive than the tip sensor. This is due to the fact that the first sensor is a set of structures connected in series that allow the existence of several optical paths that interfere with each other. However, the second sensor has higher mechanical robustness and is more practical.

5.2.5 Conclusion

Therefore, based on the table 5.2, it can conclude that the dual microsphere, taper and tip sensor, due to the existence of several optical pathways, have a higher sensitivity than the tip sensor and the latter has greater mechanical robustness. For the first sensor, the relative extremes vary non-linearly while for the tip sensor, the maximum spectrum varies linearly and the minimum varies quadratically. Both are dominated by thermal expansion.

This work shows that it is possible to produce a sensor based on the geometry of the fiber tip. These sensors allow temperature measurements in areas of the order of μm^2, presenting mechanical robustness and insensitivity to electromagnetic fields, thus allowing to respond to the need of new biological and chemical studies as well as in microstructures.

Chapter 6

Conclusion

In chapter 2, it is shown that the introduction of a light beam through the rod of the microsphere causes the generation of longitudinal and circular modes that are strongly confined within the microsphere. Is also studied the case that the center of the microsphere is not aligned with the fiber core and the case of the structure is ellipsoidal. In the first case, because the dispersion is asymmetrical, the beam that is transmitted outwards in the first air-glass reflection in the microsphere has a diagonal direction in relation to the fiber core. In the second case, the consequence is the elongation of the longitudinal modes and increase of the energy of the circular modes. In addition, it was simulated the curvature sensors where is demonstrated that the asymmetry causes an increase in the intensity of the optical paths resulting from the top and bottom of the microsphere, increasing the interferometry, and the cantilever where is verified the existence of a maximum that is located half in the tip and other half in the outside).

In chapter 3 is performed the characterization of the curvature sensor. This sensor consists of a microsphere placed between a taper. The performance of this sensor results from the sensitivity of the interferometric pattern inside the microsphere to the curvature of the optical fibers. The maximum sensitivity obtained for the variation in intensity is $(1.77 \pm 0.03) \times 10^{-7}\, km$ for the wavelength of $1526\, nm$ and for the interval of curvatures of $[1, 3]\ (m^{-1})$. The maximum sensitivity obtained for the wavelength displacement of the spectrum extremes is $(580 \pm 20)\ pm \cdot km$ for the wavelength of $1594.88\, nm$ and for the interval of curvatures of $[1, 3]\ (km^{-1})$.

In chapter 4, it is described a micro-cantilever in fiber optics. This is made up of a tip and a microsphere that are connected in series. This microsphere appears during the frabrication of the tip. Is shown that this sensor has two modes of operation to determine

the shape of the surface: proximity (less precise but safeguards the sensor) and contact (more precise). In addition, it is possible to determine the mechanical oscillations of a given object with a sensitivity of $0.032 \pm 0.001\ Hz^{-1}$ for frequencies up to 2 Hz.

In chapter 5, it is described the characterization of several structures regarding the variation of the external refractive index and the temperature variation. For the variation of the refractive index, the sensor that reveals the highest sensitivity is the narrow type with a value of $66.6\ r.i.u.^{-1}$. For temperature variation, for the low temperature range, the sensor with the highest sensitivity is the wide type sensor with a value of $4.47 \times 10^{-4}\ ^{o}C^{-1}$. For the high temperature range, the most sensitive sensor is the dual-microsphere, taper and tip with a sensitivity of $1.74 \times 10^{-5}\ ^{o}C^{-1}$. Is demonstrated that the finest and longest structures are the most sensitive to the variation of the external refractive index due to the light beam confinement being smaller. In addition, the wider and longer structures are the most sensitive to temperature variation due to the greater impact of thermal expansion.

Thus, with this work can be concluded that the use of the microsphere, despite two great features being the dispersion and the strong confinement, reveals great sensitivity to the directionality of the input and output beam and allows widening the beam diameter, increasing the multimodal characteristic of the structure that are connected in series. In addition, the use of electric arc manufacturing gives rise to structures that have greater mechanical robustness allowing increased durability of the sensor.

This work opens the door to the development of structures that, although little known, reveal a sensitivity equal to or higher than the existing ones. For future work, arise the following ideas:

- On the basis of chapter 2, namely with asymmetrical dispersion of the light beam, there is a possibility of light coupling between two fibres perpendicular to each other;
- Change the geometry dimensions of the structures that compose the sensors as well as the use of different geometries;
- Explore new applications as well as simplify the geometries used;
- Start the development of structures with the logical processing capability.

Appendix A

Simulation code in python

```
import numpy as np
import matplotlib.pyplot as plt
from scipy import interpolate
from matplotlib import cm

def V_0(X, Y, V0, R0, R1, R2):

    V = np.zeros_like(X)
    V2 = np.zeros_like(X)

    e , f =np.where(X**2/a**2 + Y**2/b**2 <(R0-R1)**2)
    f ,e= f[np.where(e<=min(f))],e[np.where(e<=min(f))]

    c,d=np.where(Y**2<R2**2)
    c,d=c[np.where(c<=min(e))],d[np.where(c<=min(e))]

    c2,d2=np.where(Y**2<(R2-R1)**2)
    c2,d2=c2[np.where(c2<len(V[0])/2)],d2[np.where(c2<len(V[0])/2)]

    for i in range(len(c)):
         V[c[i]][d[i]]= -V0 * 0.7

    for i in range(len(c2)):
```

```
        V[c2[i]][d2[i]]= -V0

    V[np.where((X)**2/a**2 + Y**2/b**2 <R0**2)] = -V0


    for i in range(len(V)):
        for j in range(len(V[0])):
            V2[i][j] = V[len(V)-i-1][j]

    return V2

plt.rc('font', family='Times New Roman', size='12')

V0=1.0e3
R0=0.125  #sphere radius
R1=(0.125 - 0.008)/2  #wall thickness
R2=0.125/2  #fiber radius

a=1.2
b=1

Z=10
N=2**Z
L=1.0
dh=2.0*L/(N-1)

X,Y=np.mgrid[-L:L+dh:dh,-L:L+dh:dh]

#Potential
V = V_0(X,Y,V0, R0,R1,R2)

#simulation parameters
dt=2.0e-5 #integration time step
```

```
omega=2 * np.pi * 1/dt / 200
N_strides=1300
M_steps=30
Pt=np.zeros(N_strides)

k_line=np.fft.fftfreq(N,dh)
Kx,Ky=np.meshgrid(k_line,k_line)
K2=Kx**2+Ky**2

#inject light into the fiber
X0= 0.50
dX=0.01
Y0=0.0
dY=0.125/8
lw=1.5*10**-2
k_w=2*np.pi/lw

fi = V0/(10**5)*(np.exp(-((X-X0)**2/dX**2+(Y-Y0)**2/dY**2)))*np.exp(-1j*k_w*X)

#graphics

y = np.round(np.linspace(np.min(Y),np.max(Y),5), decimals = 1)
x = np.round(np.linspace(np.min(X),np.max(X),5), decimals = 1)

plt.clf()
plt.contourf(X,Y,V,100, cmap='jet')
plt.ylim((np.min(Y),np.max(Y)))
plt.yticks(y,y)
plt.xlim((np.min(X),np.max(X)))
plt.xticks(x,x)
plt.xlabel('x (mm)')
plt.ylabel('y (mm)')
```

```
cbar = plt.colorbar()
cbar.ax.set_ylabel('Power (a.u.)', rotation=270, labelpad=14)
plt.show()

a = 40 * len(V) // 100
b = 60 * len(V) // 100 + 1

a1 = 40 * len(V) // 100
b1 = 60 * len(V) // 100 +1

V1 = np.delete(V[a1:b1],np.insert(np.arange(0,a+1,1),-1, np.arange(b,len(V),1)),1)
X1 = np.delete(X[a1:b1],np.insert(np.arange(0,a+1,1),-1, np.arange(b,len(X),1)),1)
Y1 = np.delete(Y[a1:b1],np.insert(np.arange(0,a+1,1),-1, np.arange(b,len(Y),1)),1)

y1 = np.round(np.linspace(np.min(Y1),np.max(Y1),5), decimals = 1)
x1 = np.round(np.linspace(np.min(X1),np.max(X1),5), decimals = 1)

plt.clf()
plt.contourf(X1,Y1,V1,100, cmap='jet')
plt.ylim((np.min(Y1),np.max(Y1)))
plt.yticks(y1,y1)
plt.xlim((np.min(X1),np.max(X1)))
plt.xticks(x1,x1)
plt.xlabel('x (mm)')
plt.ylabel('y (mm)')
cbar = plt.colorbar()
cbar.ax.set_ylabel('Power (a.u.)', rotation=270, labelpad=14)
plt.show()

plt.clf()
plt.contourf(X,Y,np.abs(fi)**2,100, cmap='jet')
plt.ylim((np.min(Y),np.max(Y)))
plt.yticks(y,y)
```

```
plt.xlim((np.min(X),np.max(X)))
plt.xticks(x,x)
plt.xlabel('x (mm)')
plt.ylabel('y (mm)')
cbar = plt.colorbar()
cbar.ax.set_ylabel('Power (a.u.)', rotation=270, labelpad=14)
plt.contour(X,Y,-V, 15, colors = 'black',linewidths=0.1)
plt.savefig('T_9\\ta_0.png', dpi=200)

plt.clf()
lj = 10 * np.log10(np.abs(fi+10**-100)**2)
plt.contourf(X,Y,lj,100, cmap='jet')
plt.ylim((np.min(Y),np.max(Y)))
plt.yticks(y,y)
plt.xlim((np.min(X),np.max(X)))
plt.xticks(x,x)
plt.xlabel('x (mm)')
plt.ylabel('y (mm)')
cbar = plt.colorbar()
cbar.ax.set_ylabel('Power (dB)', rotation=270, labelpad=14)
plt.contour(X,Y,-V, 15, colors = 'black',linewidths=0.1)
plt.savefig('T_9\\tl_0.png', dpi=200)

#Zoom
fi1 = np.delete(fi[a1:b1],np.insert(np.arange(0,a+1,1),-1, np.arange(b,len(V),1)),1)
lj = np.delete(lj[a1:b1],np.insert(np.arange(0,a+1,1),-1, np.arange(b,len(V),1)),1)

plt.clf()
plt.contourf(X1,Y1,np.abs(fi1)**2,100, cmap='jet')
plt.ylim((np.min(Y1),np.max(Y1)))
plt.yticks(y1,y1)
plt.xlim((np.min(X1),np.max(X1)))
plt.xticks(x1,x1)
```

```
plt.xlabel('x (mm)')
plt.ylabel('y (mm)')
cbar = plt.colorbar()
cbar.ax.set_ylabel('Power (a.u.)', rotation=270, labelpad=14)
plt.contour(X1,Y1,-V1,15, colors = 'black',linewidths=0.1)
plt.savefig('T_9\\ta1_0.png', dpi=200)

plt.clf()

plt.contourf(X1,Y1,lj,100, cmap='jet')
plt.ylim((np.min(Y1),np.max(Y1)))
plt.yticks(y1,y1)
plt.xlim((np.min(X1),np.max(X1)))
plt.xticks(x1,x1)
plt.xlabel('x (mm)')
plt.ylabel('y (mm)')
cbar = plt.colorbar()
cbar.ax.set_ylabel('Power (dB)', rotation=270, labelpad=14)
plt.contour(X1,Y1,-V1,15, colors = 'black',linewidths=0.1)
plt.savefig('T_9\\tl1_0.png', dpi=200)

#first half step in Fourier's space
fi = np.fft.fft2(fi)
fi = np.exp( -1.0j * 0.5 *  0.5 * K2 * dt) * fi

# integration solution
for n in range(N_strides):


    for m in range(M_steps):
        t+=dt

        #complete step into direct space
```

```
        fi = np.fft.ifft2(fi)

        for i in range(len(fi)):
            for j in range(2):
                fi[0+j][i] = 0+0j
                fi[len(fi)-1-j][i] = 0+0j

        fi=np.exp(-1.0j *  V * dt) * fi + V0/(10**5)*(np.exp(-((X-X0)**2/dX**2+(Y-Y0)**

        for i in range(len(fi)):
            for j in range(3):
                fi[0+j][i] = 0+0j
                fi[len(fi)-1-j][i] = 0+0j

        #complete step into Fourier space
        fi = np.fft.fft2(fi)
        fi = np.exp(-1.0j * 0.5 * K2 * dt) * fi


    #Last step in direct space
    fi = np.fft.ifft2(fi)
    fi = np.exp( -1.0j * V * dt) * fi

    #Last half step in Fourier space
    fi = np.fft.fft2(fi)
    fi = np.exp( -1.0j * 0.5 * 0.5 * K2  * dt) * fi

    #direct space passage
    fi = np.fft.ifft2(fi)


    #graphics
```

```
plt.clf()
plt.contourf(X,Y,np.abs(fi)**2,100, cmap='jet')
Pt[n]=np.sum(np.abs(fi)**2)
plt.ylim((np.min(Y),np.max(Y)))
plt.yticks(y,y)
plt.xlim((np.min(X),np.max(X)))
plt.xticks(x,x)
plt.xlabel('x (mm)')
plt.ylabel('y (mm)')
cbar = plt.colorbar()
cbar.ax.set_ylabel('Power (a.u.)', rotation=270, labelpad=14)
plt.contour(X,Y,-V, 15, colors = 'black',linewidths=0.1)
plt.savefig('T_9\\ta_'+str(n+1)+'.png', dpi=200)

plt.clf()
lj = 10 * np.log10(np.abs(fi+10**-100)**2)
plt.contourf(X,Y,lj,100, cmap='jet')
plt.ylim((np.min(Y),np.max(Y)))
plt.yticks(y,y)
plt.xlim((np.min(X),np.max(X)))
plt.xticks(x,x)
plt.xlabel('x (mm)')
plt.ylabel('y (mm)')
cbar = plt.colorbar()
cbar.ax.set_ylabel('Power (dB)', rotation=270, labelpad=14)
plt.contour(X,Y,-V, 15, colors = 'black',linewidths=0.1)
plt.savefig('T_9\\tl_'+str(n+1)+'.png', dpi=200)

#Zoom
fi1 = np.delete(fi[a1:b1],np.insert(np.arange(0,a+1,1),-1, np.arange(b,len(fi),1)),1)
lj = np.delete(lj[a1:b1],np.insert(np.arange(0,a+1,1),-1, np.arange(b,len(lj),1)),1)

plt.clf()
```

```
    plt.contourf(X1,Y1,np.abs(fi1)**2,100, cmap='jet')
    plt.ylim((np.min(Y1),np.max(Y1)))
    plt.yticks(y1,y1)
    plt.xlim((np.min(X1),np.max(X1)))
    plt.xticks(x1,x1)
    plt.xlabel('x (mm)')
    plt.ylabel('y (mm)')
    cbar = plt.colorbar()
    cbar.ax.set_ylabel('Power (a.u.)', rotation=270, labelpad=14)
    plt.contour(X1,Y1,-V1,15, colors = 'black',linewidths=0.1)
    plt.savefig('T_9\\ta1_'+str(n+1)+'.png', dpi=200)

    plt.clf()
    plt.contourf(X1,Y1,lj,100, cmap='jet')
    plt.ylim((np.min(Y1),np.max(Y1)))
    plt.yticks(y1,y1)
    plt.xlim((np.min(X1),np.max(X1)))
    plt.xticks(x1,x1)
    plt.xlabel('x (mm)')
    plt.ylabel('y (mm)')
    cbar = plt.colorbar()
    cbar.ax.set_ylabel('Power (dB)', rotation=270, labelpad=14)
    plt.contour(X1,Y1,-V1,15, colors = 'black',linewidths=0.1)
    plt.savefig('T_9\\tl1_'+str(n+1)+'.png', dpi=200)

    #continua a corrida
    fi = np.fft.fft2(fi)
    fi = np.exp( -1.0j * 0.5 * 0.5 * K2 * dt) * fi

plt.show()
```

Bibliography

[1] M. Henry and D. Clarke, "The self-validating sensor: rationale, definitions and examples," *Control Engineering Practice*, vol. 1, no. 4, pp. 585 – 610, 1993, doi: https://doi.org/10.1016/0967-0661(93)91382-7.

[2] W. M. Steen and J. Mazumder, *Laser Material Processing*, 4th ed. Springer, 2010.

[3] G. P. Agrawal, *Fiber–Optic Communication Systems*, 4th ed. Wiley, 2010.

[4] I. R. Matias, S. Ikezawa, and J. Corres, *Fiber Optic Sensors: Current Status and Future Possibilities*. Springer, 2017.

[5] S. Wabnitz and B. Eggleton, *All-Optical Signal Processing: Data Communication and Storage Applications*. Springer, 2015.

[6] K. Hotate and T. Okugawa, "Optical information processing by synthesis of the coherence function," *Journal of Lightwave Technology*, vol. 12, no. 7, pp. 1247–1255, July 1994, doi: https://doi.org/10.1109/50.301818.

[7] D. Psaltis and N. Farhat, "Optical information processing based on an associative-memory model of neural nets with thresholding and feedback," *Opt. Lett.*, vol. 10, no. 2, pp. 98–100, Feb 1985, doi: https://doi.org/10.1364/OL.10.000098.

[8] X. Dong, H. Du, X. Sun, Z. Luo, and J. Duan, "A novel strain sensor with large measurement range based on all fiber mach-zehnder interferometer," *Sensors*, vol. 18, no. 5, 2018, doi: https://doi.org/10.3390/s18051549.

[9] B. Jia, L. He, G. Yan, and Y. Feng, "A differential reflective intensity optical fiber angular displacement sensor," *Sensors*, vol. 16, no. 9, 2016, doi: https://doi.org/10.3390/s16091508.

[10] A. Fasano, G. Woyessa, P. Stajanca, C. Markos, A. Stefani, K. Nielsen, H. K. Rasmussen, K. Krebber, and O. Bang, "Fabrication and characterization of polycarbonate microstructured polymer optical fibers for high-temperature-resistant fiber bragg grating strain sensors," *Opt. Mater. Express*, vol. 6, no. 2, pp. 649–659, Feb 2016, doi: https://doi.org/10.1364/OME.6.000649.

[11] K. Heylman, N. Thakkar, E. Horak, S. Quillin, C. Cherqui, K. Knapper, D. Masiello, and R. Goldsmith, "Optical microresonators as single-particle absorption spectrometers," *Nature Photonics*, 11 2016, doi: https://doi.org/10.1038/nphoton.2016.217.

[12] J. Wang, F. Bo, S. Wan, W. Li, F. Gao, J. Li, G. Zhang, and J. Xu, "High-q lithium niobate microdisk resonators on a chip for efficient electro-optic modulation," *Opt. Express*, vol. 23, no. 18, pp. 23 072–23 078, Sep 2015, doi: https://doi.org/10.1364/OE.23.023072.

[13] S. Anguiano, A. E. Bruchhausen, B. Jusserand, I. Favero, F. R. Lamberti, L. Lanco, I. Sagnes, A. Lemaître, N. D. Lanzillotti-Kimura, P. Senellart, and A. Fainstein, "Micropillar resonators for optomechanics in the extremely high 19–95-ghz frequency range," *Phys. Rev. Lett.*, vol. 118, p. 263901, Jun 2017, doi: https://doi.org/10.1103/PhysRevLett.118.263901.

[14] C.-H. Dong, L. He, Y.-F. Xiao, V. R. Gaddam, S. K. Ozdemir, Z.-F. Han, G.-C. Guo, and L. Yang, "Fabrication of high-q polydimethylsiloxane optical microspheres for thermal sensing," *Applied Physics Letters*, vol. 94, no. 23, p. 231119, 2009, doi: https://doi.org/10.1063/1.3152791.

[15] K. Vahala, "Optical microcavities," *Nature*, vol. 424, pp. 839–46, 09 2003, doi: https://doi.org/10.1038/nature01939.

[16] M. L. Gorodetsky, A. A. Savchenkov, and V. S. Ilchenko, "Ultimate q of optical microsphere resonators," *Opt. Lett.*, vol. 21, no. 7, pp. 453–455, Apr 1996, doi: https://doi.org/10.1364/OL.21.000453.

[17] M. S. Ferreira, J. L. Santos, and O. F. ao, "Silica microspheres array strain sensor," *Opt. Lett.*, vol. 39, no. 20, pp. 5937–5940, Oct 2014, doi: https://doi.org/10.1364/OL.39.005937.

[18] P. Hoffmann, B. Dutoit, and R.-P. Salathé, "Comparison of mechanically drawn and protection layer chemically etched optical fiber tips," *Ultramicroscopy*, vol. 61, no. 1, pp. 165 – 170, 1995, selected Papers from the 3rd International Conference on Near-Field Optics and Related Techniques.

[19] Z. Fang, S. N. Chormaic, S. Wang, X. Wang, J. Yu, Y. Jiang, J. Qiu, and P. Wang, "Bismuth-doped glass microsphere lasers," *Photon. Res.*, vol. 5, no. 6, pp. 740–744, Dec 2017, doi: https://doi.org/10.1364/PRJ.5.000740.

[20] Shu-Bin Yan, Xiao-Qian Wang, K. Ma, A. Zhang, Chen-Yang Xue, and Wen-Dong Zhang, "Fabrication and analysis optical microsphere cavity based on high q erbium-doped," in *The 8th Annual IEEE International Conference on Nano/Micro Engineered and Molecular Systems*, April 2013, pp. 957–960, doi: https://doi.org/10.1109/NEMS.2013.6559881.

[21] L. Taylor, "A comparison between the split step fourier and finite-difference method in analysing the soliton collision of a type of nonlinear schrödinger equation found in the context of optical pulses," 09 2017. [Online]. Available: https://arxiv.org/pdf/1709.04805.pdf

[22] O. V. Sinkin, R. Holzlohner, J. Zweck, and C. R. Menyuk, "Optimization of the split-step fourier method in modeling optical-fiber communications systems," *Journal of Lightwave Technology*, vol. 21, no. 1, pp. 61–68, Jan 2003, doi: https://doi.org/10.1109/JLT.2003.808628.

[23] M. Y. Lee, J. Tan, J. Y. Heng, and C. Cheeseman, "A comparative study of production of glass microspheres by using thermal process," *IOP Conference Series: Materials Science and Engineering*, vol. 205, p. 012022, jun 2017, doi: https://doi.org/10.1088/1757-899x/205/1/012022.

[24] R. M. J. Murphy, F. Lei, J. M. Ward, Y. Yang, and S. N. Chormaic, "All-optical nanopositioning of high-q silica microspheres," *Opt. Express*, vol. 25, no. 12, pp. 13 101–13 106, Jun 2017, doi: https://doi.org/10.1364/OE.25.013101.

[25] Q. K. Kieu and V. P. Veiko, "Laser fabrication of optical microspheres," vol. 5399, pp. 126 – 132, 2004, doi: https://doi.org/10.1117/12.552791.

[26] H. Yu, Q. Huang, and J. Zhao, "Fabrication of an optical fiber micro-sphere with a diameter of several tens of micrometers," *Materials*, vol. 7, no. 7, pp. 4878–4895, 2014, doi: https://doi.org/10.3390/ma7074878.

[27] S. Silva, E. G. P. Pachon, M. A. R. Franco, P. Jorge, J. L. Santos, F. X. Malcata, C. M. B. Cordeiro, and O. Frazao, "Curvature and temperature discrimination using multimode interference fiber optic structures—a proof of concept," *Journal of Lightwave Technology*, vol. 30, no. 23, pp. 3569–3575, Dec 2012, doi: https://doi.org/10.1109/JLT.2012.2222865.

[28] N. Jalili and K. Laxminarayana, "A review of atomic force microscopy imaging systems: application to molecular metrology and biological sciences," *Mechatronics*, vol. 14, no. 8, pp. 907 – 945, 2004, doi: https://doi.org/10.1016/j.mechatronics.2004.04.005.

[29] L. Zhou, M. Cai, T. Tong, and H. Wang, "Progress in the correlative atomic force microscopy and optical microscopy," *Sensors*, vol. 17, no. 4, 2017, doi: https://doi.org/10.3390/s17040938.

[30] S. Hoen, H. J. Mamin, and D. Rugar, "Thermomechanical data storage using a fiber optic stylus," *Applied Physics Letters*, vol. 64, no. 3, pp. 267–269, 1994, doi: https://doi.org/10.1063/1.111176.

[31] A. H. L. Rosa and H. D. Hallen, "Compact method for optical induction of proximal probe heating and elongation," *Appl. Opt.*, vol. 41, no. 10, pp. 2015–2019, Apr 2002, doi: https://doi.org/10.1364/AO.41.002015.

[32] S. Hosaka, T. Shintani, M. Miyamoto, A. Kikukawa, A. Hirotsune, M. Terao, M. Yoshida, K. Fujita, and S. Kämmer, "Phase change recording using a scanning near-field optical microscope," *Journal of Applied Physics*, vol. 79, no. 10, pp. 8082–8086, 1996, doi: https://doi.org/10.1063/1.362363.

[33] B. Liu, L. Yang, and Y. Wang, "Optical trapping force combining an optical fiber probe and an afm metallic probe," *Opt. Express*, vol. 19, no. 4, pp. 3703–3714, Feb 2011, doi: https://doi.org/10.1364/OE.19.003703.

[34] S. V. Beekmans and D. Iannuzzi, "Characterizing tissue stiffness at the tip of a rigid needle using an opto-mechanical force sensor," *Biomedical Microdevices*, vol. 18, no. 1, p. 15, Feb 2016, doi: https://doi.org/10.1007/s10544-016-0039-1.

[35] M. Śmietana, M. Dominik, P. Mikulic, and W. J. Bock, "Temperature and refractive index sensing with al2o3-nanocoated long-period gratings working at dispersion turning point," *Optics & Laser Technology*, vol. 107, pp. 268 – 273, 2018, doi: https://doi.org/10.1016/j.optlastec.2018.06.017. [Online]. Available: http://www.sciencedirect.com/science/article/pii/S003039921731784X

[36] T.-H. Xia, A. P. Zhang, B. Gu, and J.-J. Zhu, "Fiber-optic refractive-index sensors based on transmissive and reflective thin-core fiber modal interferometers," *Optics Communications*, vol. 283, no. 10, pp. 2136 – 2139, 2010, doi: https://doi.org/10.1016/j.optcom.2010.01.031.

[37] Y. Wang and J. F. Muth, "An optical-fiber-based airborne particle sensor," *Sensors*, vol. 17, no. 9, 2017, doi: https://doi.org/10.3390/s17092110.

[38] N. Cherkasov, A. J. Expósito, Y. Bai, and E. V. Rebrov, "Counting bubbles: precision process control of gas–liquid reactions in flow with an optical inline sensor," *React. Chem. Eng.*, vol. 4, pp. 112–121, 2019, doi: https://doi.org/10.1039/C8RE00186C.

[39] P. Gruber, M. P. C. Marques, N. Szita, and T. Mayr, "Integration and application of optical chemical sensors in microbioreactors," *Lab Chip*, vol. 17, pp. 2693–2712, 2017, doi: https://doi.org/http://dx.doi.org/10.1039/C7LC00538E.

[40] X. Li, L. V. Nguyen, Y. Zhao, H. Ebendorff-Heidepriem, and S. C. Warren-Smith, "High-sensitivity sagnac-interferometer biosensor based on exposed core microstructured optical fiber," *Sensors and Actuators B: Chemical*, vol. 269, pp. 103 – 109, 2018, doi: https://doi.org/10.1016/j.snb.2018.04.165.

[41] M. S. A. Gandhi, S. Chu, K. Senthilnathan, P. R. Babu, K. Nakkeeran, and Q. Li, "Recent advances in plasmonic sensor-based fiber optic probes for biological applications," *Applied Sciences*, vol. 9, no. 5, 2019, doi: https://doi.org/10.3390/app9050949.

[42] G. Woyessa, K. Nielsen, A. Stefani, C. Markos, and O. Bang, "Temperature insensitive hysteresis free highly sensitive polymer optical fiber bragg grating humidity sensor," *Opt. Express*, vol. 24, no. 2, pp. 1206–1213, Jan 2016, doi: https://doi.org/10.1364/OE.24.001206.

[43] Z. Tian and S. Yam, "In-line abrupt taper optical fiber mach–zehnder interferometric strain sensor," *IEEE Photonics Technology Letters*, vol. 21, no. 3, pp. 161–163, Feb 2009, doi: https://doi.org/10.1109/LPT.2008.2009360.

[44] H.-E. Joe, H. Yun, S.-H. Jo, M. B. Jun, and B.-K. Min, "A review on optical fiber sensors for environmental monitoring," *International Journal of Precision Engineering and Manufacturing-Green Technology*, vol. 5, no. 1, pp. 173–191, Jan 2018, doi: https://doi.org/10.1007/s40684-018-0017-6.